

**1 Physical and biological processes driving seasonal variability of Nitrate
2 budget and biological productivity in the Gabon-Congo upwelling system**

**3 Landry Junior Mbang Essome^{1,2}, Gaël Alory¹, Casimir Yelognissé
4 Da-Allada^{2,3,5}, Isabelle Dadou¹, Roy Dorgeless Ngakala^{3,4}, Guillaume
5 Morvan¹**

6 ¹Université de Toulouse, LEGOS (CNES/CNRS/IRD/UT), Toulouse, France

7 ²Laboratoire de Géosciences, de l'Environnement et Applications, Université Nationale des
8 Sciences Technologies, Ingénierie et Mathématiques, Abomey, Benin.

9 ³ Department of Oceanography and Applications, International Chair in Mathematical Physics
10 and Applications, University of Abomey-Calavi, Cotonou, Benin.

11 ⁴ Department of Oceanography and Environment, Institut National de Recherche en Sciences
12 Exactes et Naturelles, Pointe-Noire, Congo.

13 ⁵Laboratoire d'Hydrologie Marine et Côtière, Institut de Recherches Halieutiques et
14 Océanologiques du Bénin, Cotonou, Bénin.

15 **Corresponding author** : L.J. Mbang Essome (landrymbangessome@gmail.com)

16

17

18

19

20

21

22

23

24

25

26

27

28

29

30

31

32

33 Acronyms:**34 CTW: Coastally trapped waves****35 CoUS: Gabon-Congo Upwelling System****36 EKW: Equatorial Kelvin Waves****37 GG: Gulf of Guinea****38 MLD: Mixed Layer Depth****39 SST: Sea Surface Temperature****40 SSH: Sea Surface Height****41 SLA: Sea Level Anomaly****42 CHLa: Chlorophyll-a****43 EBUS: Eastern Boundary Upwelling System****44 TAUS: Tropical Angolan Upwelling System****45****46****47****48****49****50****51****52****53****54****55****56****57****58****59****60****61****62****63****64****65****66**

67 Abstract

68 The Gabon-Congo upwelling system, located in the southeastern Gulf of Guinea, is a highly
69 productive marine ecosystem influenced by both local and remote physical forcing. This study
70 investigates the seasonal variability of the nitrate budget and biological productivity in this region
71 using a high-resolution (1/36°) coupled physical-biogeochemical simulation with the NEMO-PISCES
72 model. The analysis highlights the relative contributions of physical and biological processes in
73 modulating nitrate concentrations in both the mixed layer and the euphotic zone. Results reveal a
74 semi-annual cycle of nitrate, with two upwelling periods (May–August and December) and two
75 downwelling periods (January–April and October–November). These cycles are primarily driven by
76 the passage of coastal trapped waves (CTWs) forced by equatorial Kelvin waves, inducing vertical
77 thermocline displacements and regulating nitrate availability in the euphotic zone.

78 The nitrate budget analysis shows that the vertical diffusion linked to internal tide and local wind , and
79 vertical advection linked to the CTWs, are the dominant process supplying nitrate to the mixed layer
80 during the main upwelling season. However, near the Congo River mouth (5.5°S–6°S), the horizontal
81 advection plays a key role, supplying significant amounts of nitrate through the river plume. In the
82 lower euphotic layer, the vertical mixing contributes to the nitrate loss during the upwelling but
83 becomes a source of nitrate during the downwelling periods. The seasonal cycle of the chlorophyll-a
84 (CHLa) concentration follows that of nitrate, confirming that the primary production in this region is
85 mainly driven by nitrate availability. The study also highlights the role of the Angola Current in
86 transporting low-nitrate waters from the Equatorial Undercurrent, which influences the nitrate and
87 CHLa balance in the Gabon-Congo upwelling system.

88 These findings provide new insights into the mechanisms governing nutrient dynamics and biological
89 productivity in the Gabon-Congo upwelling system. Understanding these processes is crucial for
90 assessing the impact of climate variability on the regional marine ecosystems and fisheries.

91 **Keywords:** Nitrate Budget, Gabon-Congo Upwelling System, NEMO-PISCES Model,
92 Physical-Biogeochemical Interactions, Seasonal Variability, Coastal Trapped Waves

93

94

95

96

97

98

99

100

101 1 Introduction

102 The Eastern Boundary Upwelling Systems (EBUS) are the most productive areas in the global ocean
103 in terms of biological resources, hosting almost 20% of the world's fisheries (Chavez and Messie,
104 2009, 2015), even though they only represent around 1% of the world's ocean surface (Freon et al.,
105 2009). They are therefore an important economic support for the countries bordering these areas (Carr
106 et al., 2002). EBUS are controlled by wind stress blowing parallel to the coast, generating an offshore
107 Ekman transport leading to coastal upwelling of cold and nutrient-rich waters, which trigger primary
108 production in the euphotic layer, with increased surface chlorophyll-a (CHLa) concentration visible on
109 satellite images (e.g. Gutknecht et al., 2013). Besides their ecological richness, EBUS act as active
110 interfaces for greenhouse gases. They are recognized as significant sources of N_2O , primarily due to
111 the oxygen minimum zone (OMZ) that favors subsurface production (Gutknecht et al., 2013;
112 Resplandy et al., 2024). Regarding CO_2 , while cold surface waters enhance gas solubility, the vigorous
113 upwelling of deep waters rich in Dissolved Inorganic Carbon (DIC) generally dominates this thermal
114 effect, driving net CO_2 outgassing near the coast (Resplandy et al., 2024).

115 Beyond these EBUS, recent studies (Bachèlery et al., 2016; Kopte et al., 2017; Awo et al., 2022) have
116 shown that the variability of Sea Surface Temperature (SST, a key upwelling indicator) at the eastern
117 boundary of the South Atlantic was not only impacted by local wind forcing, but also by remote
118 forcing initiated by the equatorial dynamics. Indeed, the equatorial Kelvin waves (EKW) propagating
119 along the equator and later poleward along the coast as coastal trapped waves (CTW) have been shown
120 to lead to the establishment of seasonal upwelling systems.

121 This is the case for the Gabon-Congo and Angolan tropical upwelling systems, located in the
122 south-east of the Gulf of Guinea (GG), which are highly productive marine ecosystems (Ostrowski et
123 al., 2009). Fishing provides around 25% of the Angolan population's total animal protein intake and is
124 essential for economic security (Hutchings et al., 2009; Sowman and Cardoso, 2010; FAO, 2022). The
125 seasonal variability of SST along the Angolan coast has shown an evolution that was similar to that
126 observed in the Congo (Bachèlery et al., 2015, 2016; Kopte et al., 2017; Awo et al., 2022; Brandt et al.,
127 2023). It was characterized by a semi-annual pattern with an initial warming in February-April
128 followed by a first upwelling-induced cooling in May-August. Then there was a second warming, less
129 significant than the first, in September-November, followed by a second, less significant cooling in
130 December-January. Following to Radenac et al. (2020) and Brandt et al. (2023), in the tropical Atlantic
131 ocean, the thermocline and nitracline were often found at the same depth, which meant that an upward
132 movement of the thermocline was associated with upward advection of nitrate, fueling biological
133 productivity. Brandt et al. (2023) also pointed out that in the Angolan tropical upwelling system, the
134 seasonal cycle of nitrate was in phase with that of CHLa derived from ocean color satellites (Fig. 1).
135 Given that the wind stress along the coast was low for most of the year and out of phase with the

136 upwelling period, the upwelling was rather shown to be induced by the passage of waves trapped at the
137 coast, which signature was visible on the seasonal cycle of the sea level anomaly (Bachèlery et al.,
138 2016; Awo et al., 2022; Brandt et al., 2023).

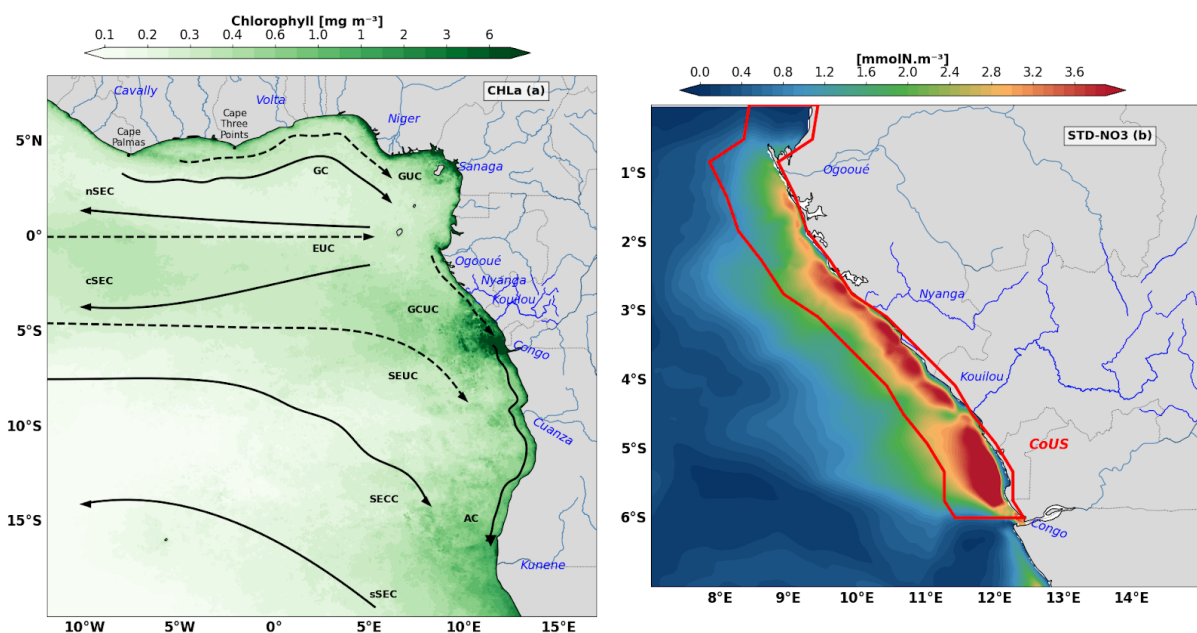
139 The cross-shore extension of the zone covered by upwelling was modulated by the regional ocean
140 circulation (Fig. 1), dominated by the southward coastal Angola Current and Congo-Gabonese
141 Undercurrent (Kopte et al., 2017; Bachèlery et al., 2016; Awo et al., 2022). Bachèlery et al. (2016),
142 based on a coupled physical-biogeochemical model, showed that equatorial remote forcing was
143 dominant for the interannual variability of nutrients and primary production, whereas the local wind
144 stress forcing was dominant for the sub-seasonal variability. Some studies also highlighted the
145 important role played by turbulent mixing, locally enhanced in shallow waters near the coast (Körner
146 et al., 2023, 2024; Tchipalanga et al., 2018a; Rouault, 2012), in the seasonal modulation of SST and
147 nutrients in Angolan coastal waters.

148 The Gabon-Congo upwelling zone (from 0°N to 6°S) is poorly documented. In a recent study using a
149 high resolution (1/36°) simulation of the NEMO model over the GG, Ngakala et al. (2025) assessed
150 the seasonal mixed layer heat budget in the Congolese upwelling system. They found that the mixed
151 layer heat budget in the Congolese coastal area was driven by two major processes: warming by heat
152 fluxes, dominated all year long by the solar flux, and cooling by vertical mixing at the base of the
153 mixed layer. whereas the total advection contribution is less important, it play a secondary role in the
154 mixed layer heat budget. However, below the mixed layer, vertical advection by upwelling CTWs was
155 crucial to raise the thermocline high enough so that cool waters can penetrate in the mixed layer by
156 vertical mixing. They also mentioned that the relative contribution of vertical advection and diffusion
157 in the mixed layer heat budget was sensitive to the criterion used to define the mixed layer.

158 These results were in agreement with the conclusion of Körner (2023) in the northern Angolan
159 upwelling south of the Congo River mouth. This latter study found that the net surface heat flux
160 warmed the coastal water further, whereas turbulent mixing across the base of the mixed layer was an
161 important cooling term. Also, Scannell and McPhaden (2018), using data from a PIRATA mooring
162 located off the Congo River at [8°E; 6°S], found that the seasonal evolution of mixed layer properties
163 had two main phases: a warm fresh phase (December-April) when solar heating was very efficient in
164 warming SST in a thin mixed layer, and a cold-salty phase (May-September) driven by the
165 intensification of southeasterly trades in response to the onset of the West African Monsoon and
166 northward displacement of the ITCZ. They also pointed out the necessity to take into account
167 precipitation influence in the mixed layer heat budget.

168 Little information has been available at the seasonal scale for biogeochemistry in the GG. In the
169 equatorial upwelling system, the respective contributions of physical and biological processes on the

170 seasonality of nitrate and biological productivity, in the mixed layer and euphotic layer, have been
 171 quantified by Radenac et al. (2020). Along the coast, most studies of biogeochemical dynamics have
 172 been either limited to the section between 6°S and the Angola Benguela frontal zone (Brandt et al.,
 173 2023), or have focused on the interannual variability of biogeochemical tracers (Bachelery et al.,
 174 2016). The seasonal variability of biogeochemical tracers and biological productivity between 0°N and
 175 6°S is likely influenced by three major processes: coastal upwelling, input of nutrients by the Congo
 176 River discharge (which is the second largest river discharge in the world; Hopkins et al., 2013), and the
 177 stratification linked to the Congo River freshwater. The aim of this paper is to investigate the
 178 respective roles of physical and biological processes in the seasonal cycle of nitrate and CHLa
 179 concentration, and the respective contributions of coastal upwelling and Congo River discharge to the
 180 biological productivity in the Gabon-Congo upwelling system. The paper is organized as follows:
 181 Section 2 describes the numerical model and datasets; Section 3 presents the model validation and the
 182 nitrate budget analysis; Section 4 discusses the physical-biological interactions, and Section 5 provides
 183 the conclusions.



184

185 **Figure 1:** Regional ocean circulation and spatial distribution of biological and nutrient tracers.

186 (a) Annual mean surface Chlorophyll-a concentration (CHLa, [mg m^{-3}]). The map illustrates the spatial
 187 distribution of biological productivity across the Gulf of Guinea and the South Atlantic African margin. Black
 188 arrows and dashed lines indicate the major surface and subsurface currents: northern, central and southern
 189 branches of the South Equatorial Current (nSEC, cSEC and sSEC , respectively), Equatorial Undercurrent
 190 (EUC), Guinea Current (GC), Guinea Undercurrent (GUC), Gabon-Congo Undercurrent (GCUC), South
 191 Equatorial Undercurrent (SEUC), South Equatorial Counter Current (SECC), and Angola Current (AC). (b)
 192 Standard deviation of Nitrate concentration (STD-NO3, [mmolN m^{-3}]). The color scale represents the
 193 variability of nitrates in the upper ocean. The red polygon delimits the coastal domain defined as the
 194 Gabon-Congo Upwelling System (CoUS), extending from the Congo River mouth ($\sim 6^\circ\text{S}$) to the Equator ($\sim 0^\circ\text{S}$),

195 which serves as the primary study area for the nutrient budget analysis. Blue labels highlight the discharge points
196 of the Ogooué, Nyanga, Kouilou, and Congo rivers.

197 **2 Data and methods**

198 **2.1 Numerical model**

199 To understand the dynamics in the Gabon-Congo upwelling system, we have used the NEMO
200 (Nucleus for European Modelling of the Ocean) ocean general circulation model based on the
201 primitive equations discretized on an Arakawa-C grid (Madec et al., 2024). The vertical mixing is
202 computed from a turbulent closure scheme using the GLS (Generic Length Scale) formulation.

203 In this work, the NEMO model was coupled with PISCES (Pelagic Interactions Scheme for
204 Carbon and Ecosystem Studies), a biogeochemical model developed by Aumont et al. (1998) and
205 subsequently improved. Here, the version used is PISCES-2 (Aumont et al., 2015). This model has
206 three main compartments: the first represents nutrients, including nitrogen compounds (nitrate and
207 ammonium), iron, phosphate and silicates; the second represents phytoplankton and includes two
208 classes, nano-phytoplankton and diatoms; the third compartment represents zooplankton, made up of
209 two classes, microzooplankton and meso-zooplankton. We used the PISCES (cell quotas) model with
210 constant Redfield ratios (Aumont and Bopp, 2006; Aumont et al., 2015).

211 A regional configuration of the GG (11°S - 6°N; 10°W - 14°E) with an horizontal resolution
212 of 1/36° and 50 vertical levels is used. The atmospheric forcing is derived from the JRA-55 reanalysis
213 of the Japanese meteorological agency (Kobayashi et al. 2015), except for the wind forcing which is
214 based on daily ASCAT (Advanced SCATterometer) satellite data at 1/4° spatial resolution. Lateral
215 boundaries conditions are from Mercator GLORYS12V1 reanalysis data at 1/12° spatial resolution for
216 physics and NEMO-PISCES reanalysis at 1/4° of Radenac et al. (2020) for biogeochemistry.
217 Continental freshwater inputs for this configuration are derived from the ISBA-CTRIP model, and in
218 situ data from the HYBAM network for the Congo River. The NEMO configuration, ran over the
219 period 2007-2017 (after a two-year spin-up), was validated by Ngakala et al. (2025) in our region of
220 study. This simulation has also been validated and used in the Northern Gulf of Guinea for the coastal
221 upwelling in summer and its interaction with mesoscale dynamics (Thiam et al., 2024). The reference
222 simulation of the coupled biogeochemical physical model (NEMO-PISCES) was produced over the
223 period 2007-2011, with a spin-up of 4 years for the biogeochemical part (2007-2010). We analysed
224 monthly and daily outputs for the year 2011, which is characterised by neutral conditions regarding the
225 Atlantic Niño and Benguela Niño interannual variability (Brandt et al., 2023).

226 .

227

228 2.2 Satellite and in-situ data

229 Several observational products were used to assess the model's ability to reproduce the physical and
 230 biogeochemical characteristics of the area for the year 2011. We used the MUR product (Multi-scale
 231 Ultra-high Resolution; Chin et al., 2017) with $1/4^\circ$ spatial resolution and daily temporal resolution to
 232 assess the regional distribution and the seasonal cycle of SST. The vertical temperature distribution
 233 was assessed using the World Ocean Atlas (WOA; Locarnini et al., 2018; Zweng et al., 2019)
 234 climatology. The CHLa data used came from the Globcolour product distributed by Copernicus Marine
 235 Environment Monitoring Service (<http://marine.copernicus.eu/>), which combines data from four ocean
 236 color satellites, with very high spatial resolution (1 km) and daily temporal resolution.

237 The nutrient fields were assessed using the CSIRO Atlas of Regional Seas climatology
 238 (Ridgway and Dunn, 2002) which merges several in situ databases (Argo buoys, WOD2005, WOCE3,
 239 Global Hydrographic Program, CTD and CMAR4 hydrology archives, NIWA5 hydrographic data, and
 240 CRC6 hydrographic data). It provides physical variables (Temperature, Salinity) and biogeochemical
 241 variables (NO_3 , PO_4 , O_2 , Si) both at the surface and at depth with a horizontal resolution of $1/2^\circ$, 79
 242 vertical levels from the surface to 5500 m depth, with a step of 5 m near the surface then increasing
 243 with depth, and a daily temporal resolution. This product was built from 2009 and contains data from
 244 1940 until 2011 which was the date when the last revision of the product was made. Near surface
 245 currents from the Ocean Surface Current Analysis Real-time (OSCAR, Johnson et al. 2007) dataset are
 246 based on satellite and in situ measurements of sea surface height surface vector wind and SST. They
 247 are derived from quasi-linear and steady flow momentum equations thus combine geostrophic, Ekman
 248 and Stommel shear dynamics. OSCAR product is available on a $1/3^\circ \times 1/3^\circ$ grid with a 5-day temporal
 249 resolution for year 2011, and we use it to validate the near surface currents (first 30 meters) of the
 250 model outputs. Sea Level Anomaly was computed from the salto/duacs gridded product of Absolute
 251 Dynamic Topography for 2011. This product is based on sea surface height measurement of
 252 multimission altimeters since 1992, optimally interpolated onto $0.25^\circ \times 0.25^\circ$ longitude/latitude grid
 253 (Ducet et al., 2000).

254 2.3 Methods

255 The variability of nutrients and in particular nitrate is driven by several physical and biogeochemical
 256 processes taken into account in our model. As in Radenac et al (2020), the nitrate budget integrated
 257 over the mixed layer depth is represented by the following equation:

$$\begin{aligned}
 & \frac{\partial \langle NO_3 \rangle}{\partial t} = - \langle u \frac{\partial NO_3}{\partial x} \rangle - \langle v \frac{\partial NO_3}{\partial y} \rangle - \langle w \frac{\partial NO_3}{\partial z} \rangle + \frac{1}{h} \left(K_z \frac{\partial NO_3}{\partial z} \right)_{z=-h} - \frac{1}{h} \frac{\partial h}{\partial t} \left(\langle NO_3 \rangle - NO_{3_{z=-h}} \right) \\
 & + SMS(NO_3) \quad (1)
 \end{aligned}$$

260 In Equation (1), the term on the left represents the total nitrate tendency, where the brackets $\langle \dots \rangle$
 261 denote the vertical average within the mixed layer of depth h . This depth h is defined as the level
 262 where the potential density exceeds the reference density at 3 meters by approximately 0.06 kg/m^3
 263 (Aroucha et al., 2025). On the right side of the equation, the first three terms represent the zonal,
 264 meridional, and vertical advectons of nitrate, respectively, with u, v and w being the components of the
 265 velocity field. The fourth term represents the vertical diffusion (mixing) at the base of the mixed layer
 266 ($z=-h$), where K_z is the vertical diffusion coefficient that varies in space and time. The fifth term
 267 corresponds to the entrainment term, which represents the flux of nitrate into the mixed layer during its
 268 deepening. However, it is not explicitly solved in our budget analysis. Following Radenac et al. (2020)
 269 for the tropical Atlantic using a similar NEMO-PISCES configuration, this term is negligible
 270 compared to other terms in the budget. Finally, the SMS (Source Minus Sink) term represents the
 271 contribution of biological processes to the spatial and temporal variability of NO_3 concentrations, as
 272 detailed in the following expression:

$$273 \text{SMS}(\text{NO}_3) = \text{Nitri}f - \mu_{\text{NO}_3}^P * P - \mu_{\text{NO}_3}^D * D - R_{\text{NH}_4} * \lambda_{\text{NH}_4} * \Delta(\text{O}_2) * \text{NH}_4 - R_{\text{NO}_3} * \text{Denit} \quad (2)$$

274 where *Nitri*f corresponds to nitrification, which is the conversion of ammonium into nitrate by
 275 bacterial activity. It is parameterized by:

$$276 \text{Nitri}f = \lambda_{\text{NH}_4} - \frac{\text{NH}_4}{1 + \langle \text{PAR} \rangle} (1 - \Delta(\text{O}_2)) \quad (3)$$

277 where NH_4 is the ammonium concentration, $\langle \text{PAR} \rangle$ is the average fraction of solar radiation available
 278 for photosynthesis, λ_{NH_4} is the nitrification rate and $\Delta(\text{O}_2)$ is the oxygen variation in the mixed layer,
 279 which provides information on the oxic and anoxic conditions of the water column: The second and
 280 third terms on the right of equation (2) are the growth of nanophytoplankton and diatoms, where $\mu_{\text{NO}_3}^P$
 281 and $\mu_{\text{NO}_3}^D$ are their growth rates, P and D are their concentrations respectively. R_{NH_4} and R_{NO_3} are the
 282 stoichiometric N/C ratios of ammonification and nitrification respectively.. *Denit* represents
 283 denitrification which occurs when the water becomes anoxic, and so nitrate (instead of oxygen) is
 284 consumed by remineralization of organic matter. A detailed description of the terms of these equations
 285 is given by Aumont et al (2015). We used the parameter PISCES values modified for the Tropical
 286 Atlantic ocean from Radenac et al. (2020). The balance terms in equation (1) have been calculated
 287 online for 2011. As the lateral diffusion term is generally negligible compared with the others, it will
 288 not be discussed further.

289 Since the advection in (1) depends on both nitrate gradients and velocities, we investigate which
 290 component primarily controls its contribution. First, we analyze the seasonal evolution of gradient and

291 velocity following Awo et al. (2022). Second, we evaluate the individual contributions of seasonal
 292 variations in velocity and gradient, as well as their combined effect, following Topé et al. (2023),
 293 according to equation (4).

$$294 \left(V_i \cdot \nabla_i (NO_3) \right)' = V_i' \cdot \overline{\nabla_i (NO_3)} + \overline{V_i} \cdot \nabla_i (NO_3)' + V_i' \cdot \nabla_i (NO_3)' \quad (4)$$

295 The total seasonal variation of the advection term is thus decomposed into three distinct contributions:

296 $V_i' \cdot \overline{\nabla_i (NO_3)}$ (Current variability), this term quantifies the impact of current velocity anomalies acting
 297 upon a mean (steady-state) nitrate distribution. It isolates the effect of current acceleration or
 298 intensification (such as the SEUC or the Angola Current) on nutrient transport. $\overline{V_i} \cdot \nabla_i (NO_3)'$ (Gradient
 299 variability), this term represents the impact of seasonal changes in the nitrate concentration gradient
 300 under a mean circulation. It highlights the influence of seasonal water mass enrichment, particularly
 301 via the Congo River plume. $V_i' \cdot \nabla_i (NO_3)'$ (Non-linear term), this term accounts for the simultaneous
 302 interaction between current fluctuations and gradient fluctuations. To determine which of these
 303 mechanisms predominantly governs the nitrate budget, Pearson correlation coefficients were
 304 calculated between the total advective anomaly and each decomposed component. This statistical
 305 approach serves a critical physical objective: it allows us to disentangle whether the seasonal nitrate
 306 supply is driven primarily by the kinematic modulation of the flow (circulation-driven) or by the
 307 pulsing of the nutrient source (supply-driven). A high correlation with the current term would identify
 308 regional circulation such as the SEUC or Angola Current as the primary pump, whereas a dominant
 309 correlation with the gradient term would pinpoint the massive periodic enrichment, particularly from
 310 the Congo River plume, as the main trigger of nitrate variability. All reported correlations are
 311 statistically significant at a 95% confidence level ($p < 0.05$). By establishing this statistical hierarchy,
 312 we can physically characterize the system as being either transport-limited or supply-limited,
 313 providing a rigorous diagnostic of the processes regulating primary productivity in the Gabon-Congo
 314 upwelling. The Primary production (NPP) was calculated from the phytoplankton evolution equation
 315 (Aumont et al 2015):

$$316 \quad NPP = (1 - \delta^P) \mu^P * P \quad (5)$$

317 In this equation, P is the phytoplankton biomass (diatoms), δ^P represents the exudation of the
 318 phytoplankton (diatoms). μ^P is the specific growth rate of the phytoplankton taking into account
 319 nutrient and light availability. Note that this equation applies to each phytoplankton species (diatoms
 320 or nanophytoplankton), and total NPP is the sum of NPP from both diatoms and nanophytoplankton.
 321 μ^P is the specific growth rate of the phytoplankton taking into account nutrient and light availability.

322 NPP, which represents the organic matter synthesized by phytoplankton after accounting for
323 autotrophic respiration, is calculated online by the coupled NEMO-PISCES model. Within the model
324 framework, NPP is partitioned into New Production (NP), fueled by external nutrient inputs (primarily
325 nitrate) through advection and diffusion, and Regenerated Production (RP), sustained by nutrients
326 recycled within the euphotic zone (primarily ammonium). Both NP and RP components are computed
327 online, providing a detailed breakdown of the trophic status and nutrient utilization efficiency in the
328 Gabon-Congo upwelling system.

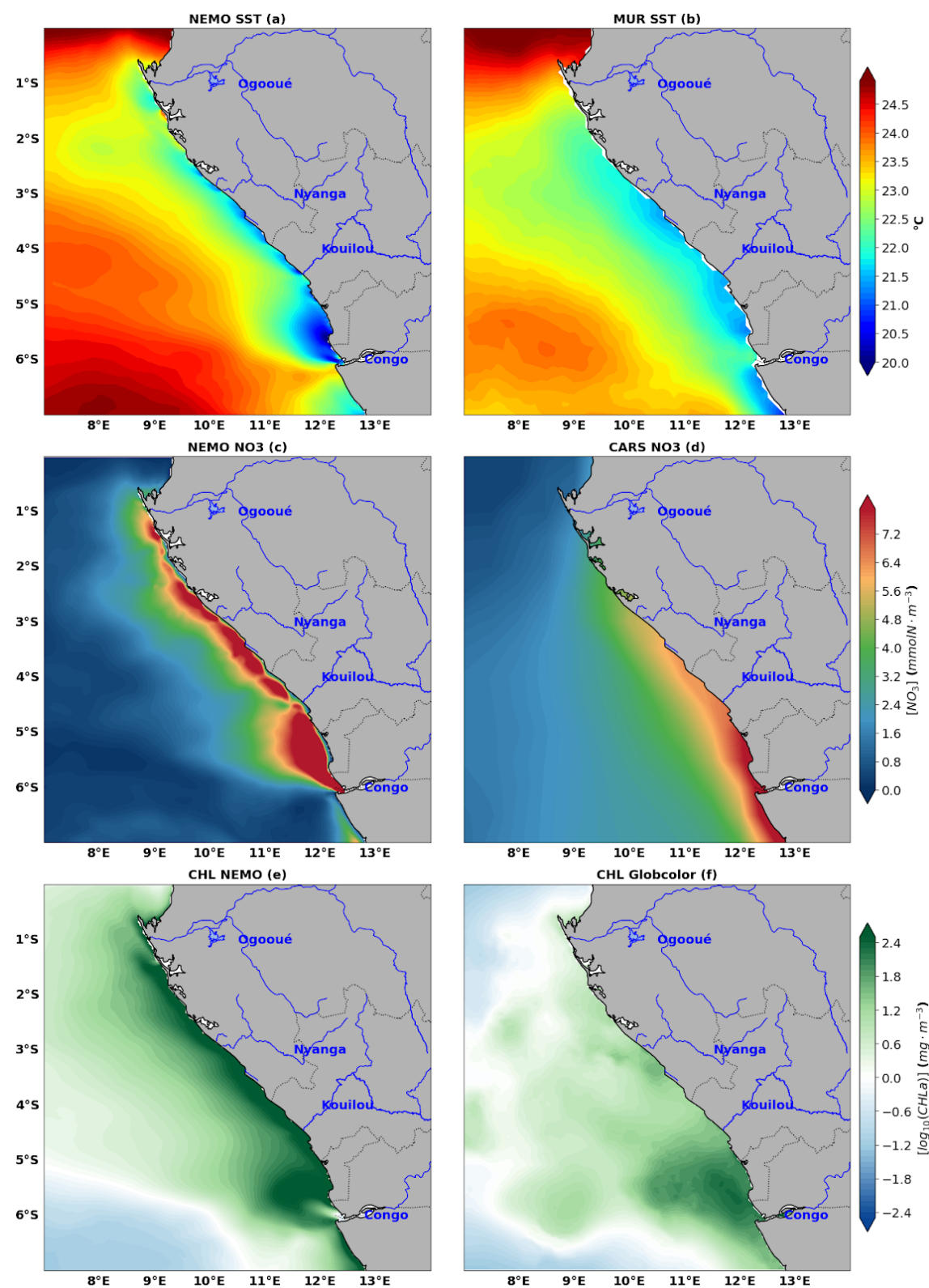
329

330 **3 RESULTS**

331 **3.1 Model/data comparison**

332 **3.1.1 Spatial variations during the upwelling period**

333 The assessment of our model simulation has been done using several observation products of physical
334 variables , including Sea Surface Temperature (SST), Sea Surface Height (SSH), and ocean currents,
335 as well as biogeochemical tracers such as nitrate (NO_3) and CHLa, based on both satellite and in situ
336 data. Fig.2 shows the regional distribution from observations and model outputs for both SST
337 (Fig.2a-b), nitrate concentration (Fig.2c-d) and CHLa concentration (Fig.2e-f), averaged for austral
338 winter (June,July and August) which is the main Gabon-Congo upwelling period (Ngakala et al.,
339 2025). As can be seen, the upwelling feature is well captured by the model with cooling of surface
340 water at the coast below 23°C in the model and 22°C in the MUR product (Fig. 2a,b). This cooling
341 feature is consistent with high nitrate (Fig. 2c,d) and CHLa (Fig. 2e,f) concentrations in both models
342 and observation, particularly north of the Congo estuary (6°S) and nearby Kouilou River mouth (Fig.
343 2e) at 4.47°S . These cool and enriched nutrient coastal waters are spread offshore displaying a
344 cross-shore gradient, with a greater extension in the observation than the model. The highest nitrate
345 concentration in the coastal waters is greater than 10 mmolN.m^{-3} in the model (8 mmolN.m^{-3} in the
346 observation) located mainly in the Congo River plume area, inducing enhancement of PP resulting in a
347 strong CHLa signature.



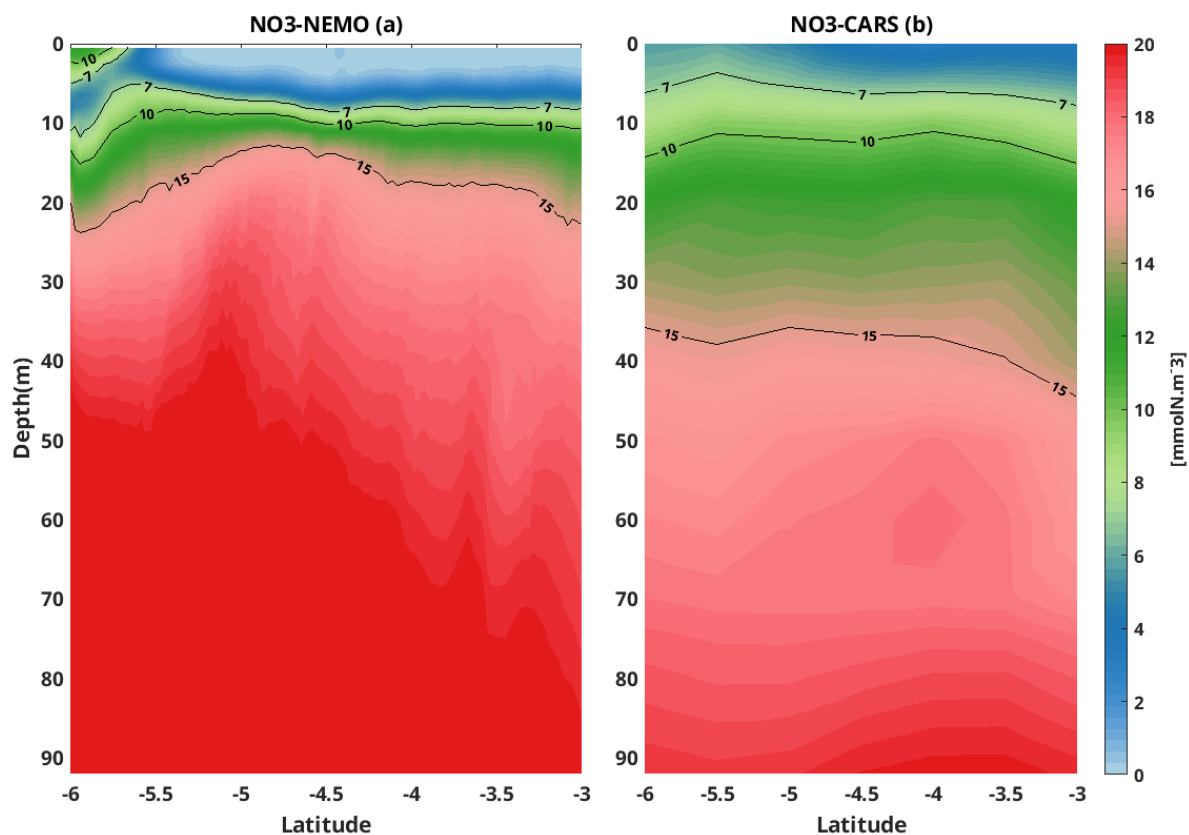
348

349 **Figure 2:** Comparison between model (left hand side) and observations (right hand side) with regional
 350 distribution of sea surface temperature (a, b), nitrate concentration (c, d) and CHLa concentration (e, f)
 351 averaged for austral winter (June, July, August)

352 The offshore area (7°E-10°E) is the oligotrophic zone characterized by relatively warm waters (24.5°C
 353 in the model and 23.5°C in the observation), depleted in nitrate and less productive in CHLa
 354 concentration. In this offshore area nitrate concentrations are lower than 1.6 mmolN.m⁻³ in the
 355 observation and 0.8 mmolN.m⁻³ in the model.

356 Although the model captures relatively well the regional distribution of the 3 variables, we can see
 357 some differences. For instance, the model is warmer than observations by about 1°C and shows
 358 stronger nitrate concentration (by about 2 mmolN.m⁻³) and CHLa concentration (6-10 mg.m⁻³) at the
 359 coast. In the offshore area, the model seems to be less enriched in nitrate concentration than the
 360 observation by about 0.8 mmolN.m⁻³.

361 High variability of nitrate concentration is found in the coastal Gabon-Congo area (Fig.1b) and in the
 362 Congo river plume zone as we can see in model annual standard deviation distribution of NO₃.
 363 Therefore the red box (0°S-6°S, 1° width coastal band) in Fig.1b is used to analyze the vertical nitrate
 364 profile to assess the model's ability to capture its vertical distribution. This area corresponds to our
 365 studied area in the Gabon-Congo coastal upwelling zone.

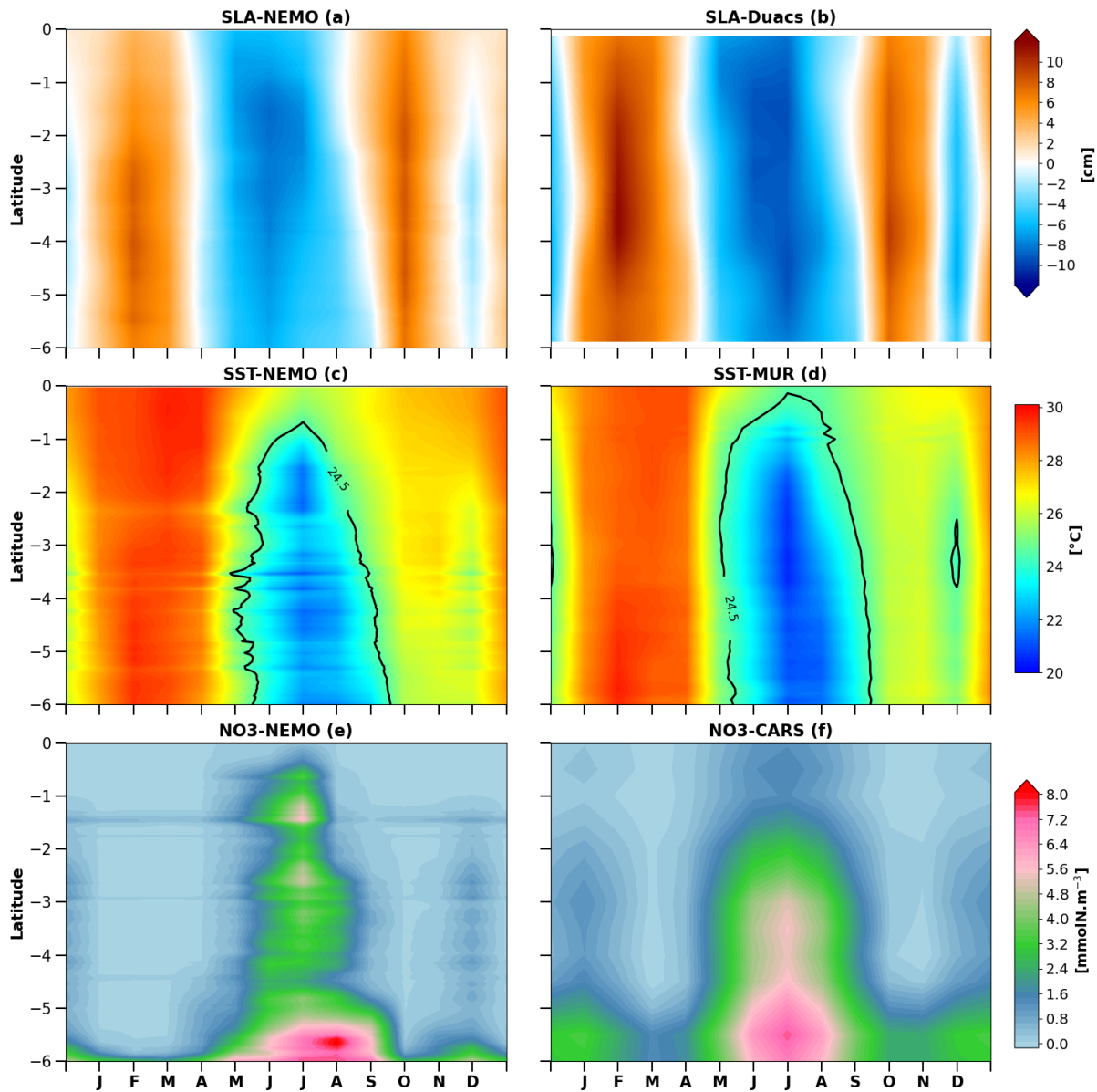


366
 367 **Figure 3:** Comparison between model (a) and observation (b) using vertical distribution of nitrate concentration
 368 in the first 90 m, in the coastal box (3°S-6°S and 1° width band to the coast) in the main upwelling season
 369 (June, July and August). black represents nitrate concentration isolines.

370 Very close to the surface, water masses are nutrient depleted for both model and observation (Fig.3),
 371 likely due to photosynthesis activity of phytoplankton that consumes nitrate in presence of light,

372 increasing its biomass thus CHLa concentrations. However this depletion is more pronounced in the
 373 model than in the observation. In the subsurface, the high nitrate concentration is due to the
 374 remineralization of organic matter by bacteria and coastal upwelling of deeper enriched nitrate waters,
 375 with the model showing higher concentrations than observed. Although nitrate isolines are shallower
 376 in the model than in observations below about 15 m depth, some nitrate isolines are relatively well
 377 captured by the model, for instance isolines 7 and 10 mmolN.m^{-3} .

378 3.1.2 Seasonal cycle of SST, nitrate, SLA and current in the Gabon-Congo coastal area



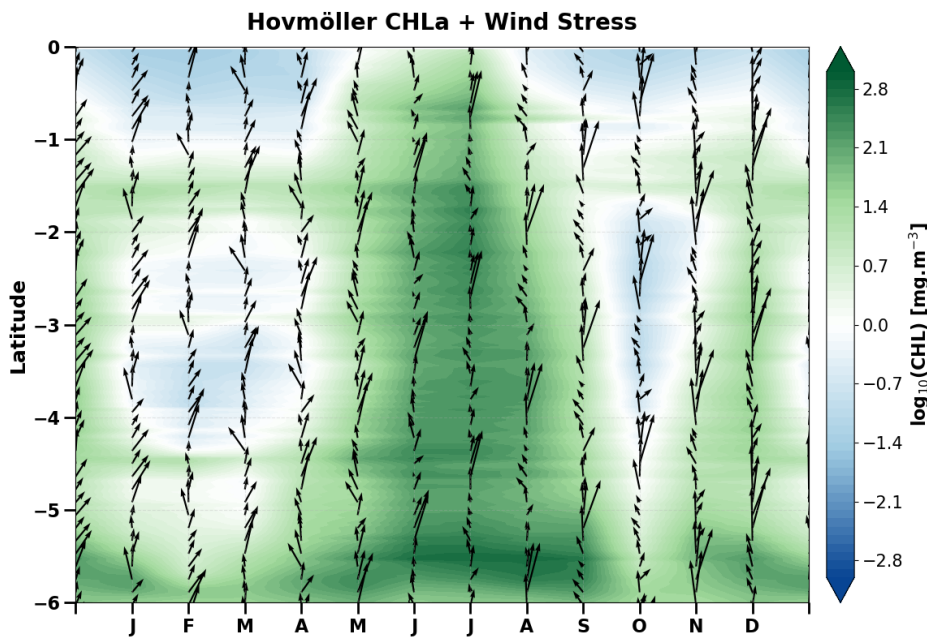
379
 380 **Figure 4:** Comparison between modeled (left) and observed (right) seasonal cycles of Sea Level Anomaly (a, b),
 381 SST(c, d) and nitrate concentration (e, f) averaged in the coastal box ($6^{\circ}\text{S}-0^{\circ}\text{S}$, 1° width).

382 Now we use the coastal box defined in Fig. 1b to evaluate the seasonal cycle of nitrate. The nitrate
 383 seasonal variability is characterized by a semi-annual cycle with two maxima and two minima in the

384 model and the observations. The main maximum occurs from May to September when SST reaches its
385 minimum of 20°C in both model and observations (Fig.4c, Fig.4d) and the secondary maximum occurs
386 in December when SST reaches a secondary minimum of 25.5°C in the model and 24.5°C in
387 observation. We have a warmer SST reaching 30°C from January to April and 26°C from October to
388 November in both the model and the observations. This semi-annual SST cycle is likely due to CTWs
389 propagation since it is consistent with the SLA seasonal cycle (minimum SST corresponds to negative
390 SLA and maximum SST corresponds to positive SLA) as mentioned earlier by Ngakala et al. (2025) in
391 the same area. Indeed, the propagation of CTWs induce vertical migration of the thermocline resulting
392 thereby in cooling or warming at the surface. At the seasonal scale, the propagation of upwelling
393 CTWs from May to September and in November-December uplifts thermocline, supplying cold waters
394 to the surface and reducing Sea Surface Height (SSH) by steric effect. As downwelling CTWs
395 propagate from January to April and in September-October, they deepen thermocline, warming the
396 surface and increasing SLA. The cold waters upwelled by CTWs (May-September) are highly
397 enriched in nitrate, whereas warm surface waters induced by downwelling CTWs (January-April and
398 September-October) are nitrate depleted. The seasonal variability of SLA due to CTWs (Fig.4a,
399 Fig.4b) is consistent with the seasonal variability of SST (Fig.4c, Fig.4d) and of nitrate concentration
400 (Fig.4e, Fig.4f) in both the model and observations. The highest nitrate concentration is around 10
401 mmol.m^{-3} near the Congo River mouth (6°S) and decreasing northward, however the observations
402 seem to be richer in nitrate than the model. In December during the secondary cooling, nitrate
403 concentration in the model is greater by about 1.2 mmol.m^{-3} than observed along the coast. In the
404 warming period (January-April and October-November), this coastal area seems to be nitrate depleted.
405 Despite the model capturing the SLA signature, the observed seasonal cycle of SLA remains more
406 intense than in the simulation. This feature is driven by the combined effect of remotely forced
407 Equatorial Kelvin Waves (EKW) and poleward-propagating CTWs (Bachèlery et al., 2016; Kopte et
408 al., 2017; Awo et al., 2023; Brandt et al., 2023). During cooling periods, upwelling CTWs decrease the
409 SLA and uplift the thermocline. Following Radenac et al. (2020), the thermocline depth in this region
410 acts as a reliable proxy for the nitracline; its upward migration significantly enhances nitrate supply to
411 the surface, fueling biological productivity. Conversely, the downwelling waves observed in the
412 warming periods increase the SLA and deepen the nitracline, leading to the nutrient-depleted
413 conditions described previously.

414 High nitrate concentrations support biological production, therefore correspond to high CHL_a signals
415 at the surface (Fig.5). On the contrary, during the warming period, the downwelling CTWs
416 propagating along the coast increase SLA, deepen the thermocline (Ngakala et al. (2025). This also
417 deepens the nitracline and consequently deplete the nitrate concentration at the ocean surface, thus the
418 low CHL_a signal (Fig.5).

419 The variability of simulated near-surface currents between 0 to 15 m depth (Fig.6) was compared to
 420 the OSCAR product. Here, we make a latitudinal section at 4°S and look at the seasonal cycle of
 421 meridional currents (Fig.6a and 6b) from 7°E to the coast for both the model (Fig.6a) and observations
 422 (Fig.6b). We do not restrict to the Gabon-Congo box as we have done for other variables, because the
 423 OSCAR product is not well resolved at the vicinity of the coast. So we can see that the model
 424 reasonably represents the seasonal variability of meridional currents with northward velocities in
 425 April, June-September and November-December with the magnitude of around 0.1 m.s⁻¹. In the
 426 observations, this structure is more or less similar, but we can see some differences: southward
 427 velocities between 8.5°E and 10.2°E in July, and also between 7°E and 9°E during August-September
 428 and January, are not found in the model.



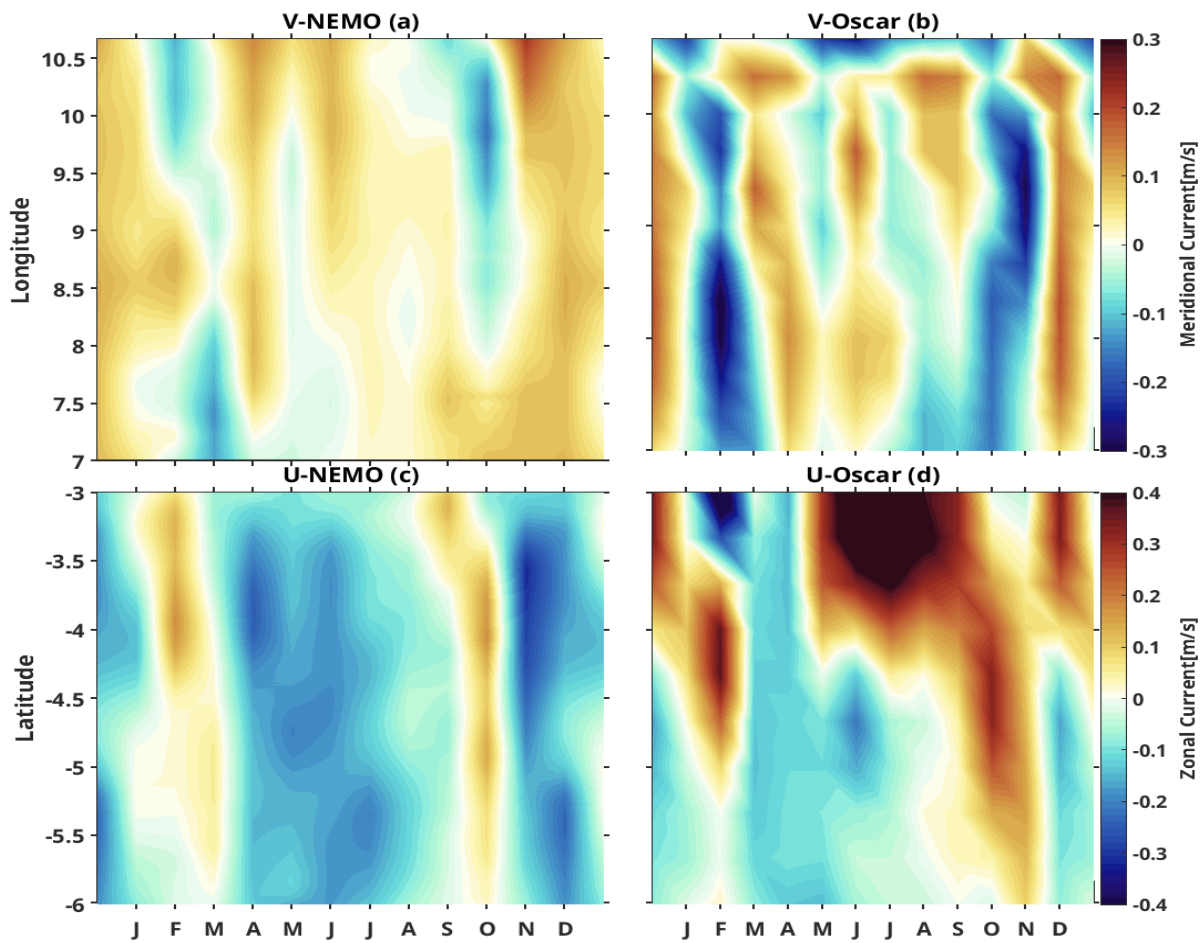
430 **Figure 5:** Seasonal cycle of CHLa concentration (in background) and wind stress (black arrow) along the
 431 Gabon-Congo coastal box (6°S-0°S, 1° width) area in the model.

432 Nevertheless, we can see in both products southward currents in February-March and October with a
 433 strong magnitude of 0.25 m.s⁻¹ in the observations though only 0.15 m.s⁻¹ in the model. This seasonal
 434 structure is consistent with the seasonal cycle of meridional currents off Angola, further south, and the
 435 southward flow in February-March and October seems to be the Angola current (Kopte et al 2017). To
 436 assess the zonal current (Fig.6c and 6d), we make a longitudinal section at 10°E and we look at the
 437 seasonal cycle of zonal current between 3°S and 7°S. The modeled zonal structure with westward
 438 velocities from April to August and November – December has a magnitude of about 0.1 m.s⁻¹ along
 439 the section (Fig.6c), in agreement with the observations (Fig.6d), which also show westward velocities
 440 from April to August. However there are some differences with the model from March to August
 441 between 3°S and 4.5°S where we can observe very strong (more than 0.5 m.s⁻¹) eastward flow. In
 442 contrast to the model, the flow during November is eastward in the observation. The noticeable

443 similitude is the eastward flow in January- February and October with a magnitude of 0.15 m.s^{-1} which
 444 seems to be the signature of the South Equatorial UnderCurrent (SEUC). This eastward current is
 445 deeper further offshore (100 m depth) west of 0°E (Bourles et al., 2004) and rising near the surface
 446 near the coast (Nubi et al., 2016; Assene et al., 2022).

447 3.2 Nitrate budget in the mixed layer

448 Generally, the seasonal variations in CHLa are thought to be primarily related to seasonal variations of
 449 the nitrate input in the equatorial Atlantic ocean (Loukos and Mémerly., 1999; Radenac et al, 2020) and
 450 in the tropical Angolan upwelling (Brandt et al., 2023). This is probably the case also in the
 451 Gabon-Congo coastal area, where the seasonal cycles of nitrate (Fig.7a) and CHLa (Fig.5) in our
 452 model are very consistent. Corresponding to the semi-annual variability of nitrate, the seasonal change
 453 rate of its concentration (Fig. 8b) displays a four-phase cycle: a first increasing phase between March
 454 and August with a highest amplitude ($0.3 \text{ mmol.m}^{-3}.\text{d}^{-1}$) in July, followed by a decreasing phase in
 455 Spetember –November with a highest amplitude in October ($0.01 \text{ mmol.m}^{-3}.\text{d}^{-1}$ north of 5°S and about
 456 -0.13 to $-0.3 \text{ mmol.m}^{-3}.\text{d}^{-1}$ between 5°S and 6°S all years long).



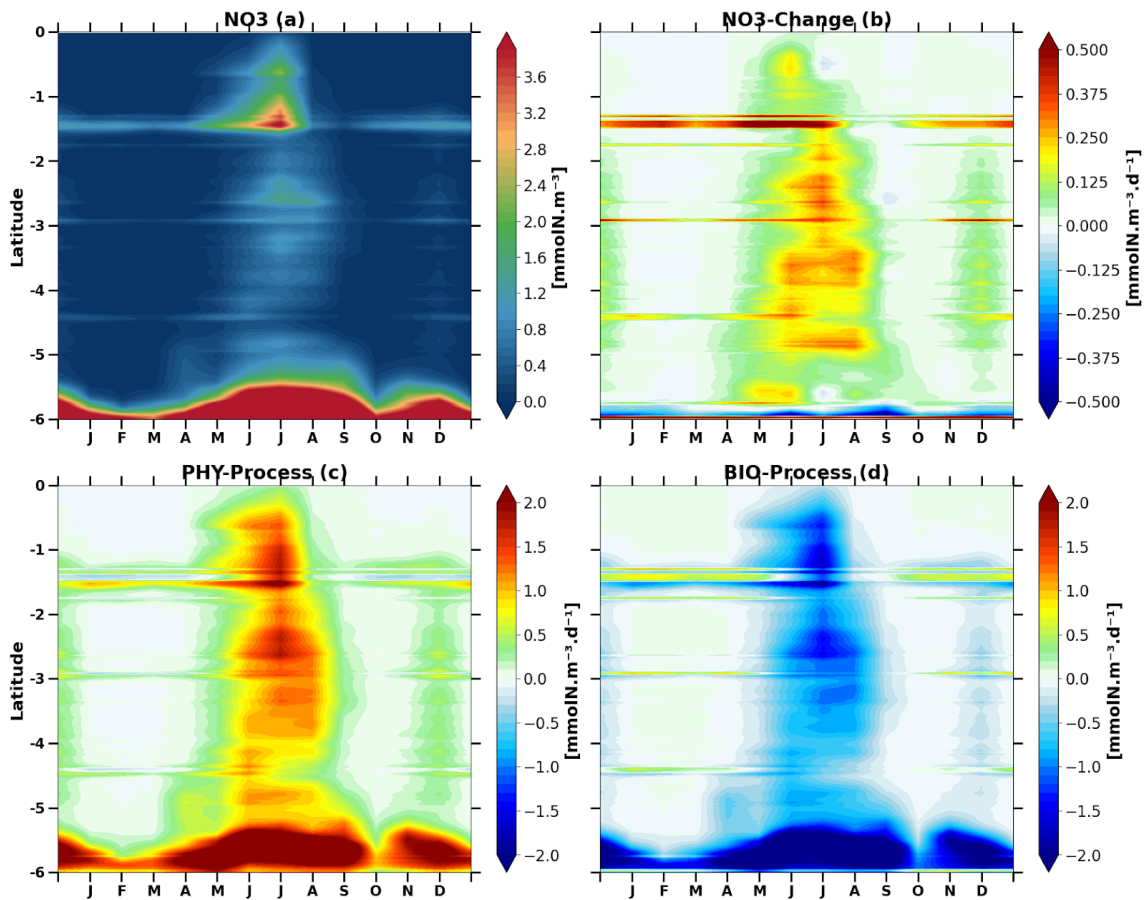
457

458 **Figure 6:** Seasonal cycle of surface current, zonal current (a, b) at 10°E section and between 3°S and 7°S
 459 meridional current (c, d) at 4°S section from 7°E to the coast.

460 Then we have a weak second increasing phase in November-December of about $0.1 \text{ mmol.m}^{-3}.\text{d}^{-1}$ and a
 461 weak decreasing phase in January- February ($0.01 \text{ mmol.m}^{-3}.\text{d}^{-1}$). This semi-annual cycle is due to a
 462 balance between nitrate supply by physical processes (Fig.7c), maximum during the main upwelling
 463 period, and nitrate consumption by biological processes (Fig.7d).

464 3.2.1 Seasonal Nitrate Budget Analysis: Horizontal Vs Vertical Contributions

465 Looking at our previous results, we saw that physical processes drive the nitrate supply in the
 466 Gabon-Congo upwelling system, now we will look at the contribution of horizontal and vertical
 467 processes to understand which are the main drivers for this nitrate supply. Fig.8 shows that horizontal
 468 and vertical processes (Fig.8a and Fig.8b respectively) are of great importance for nitrate supply.

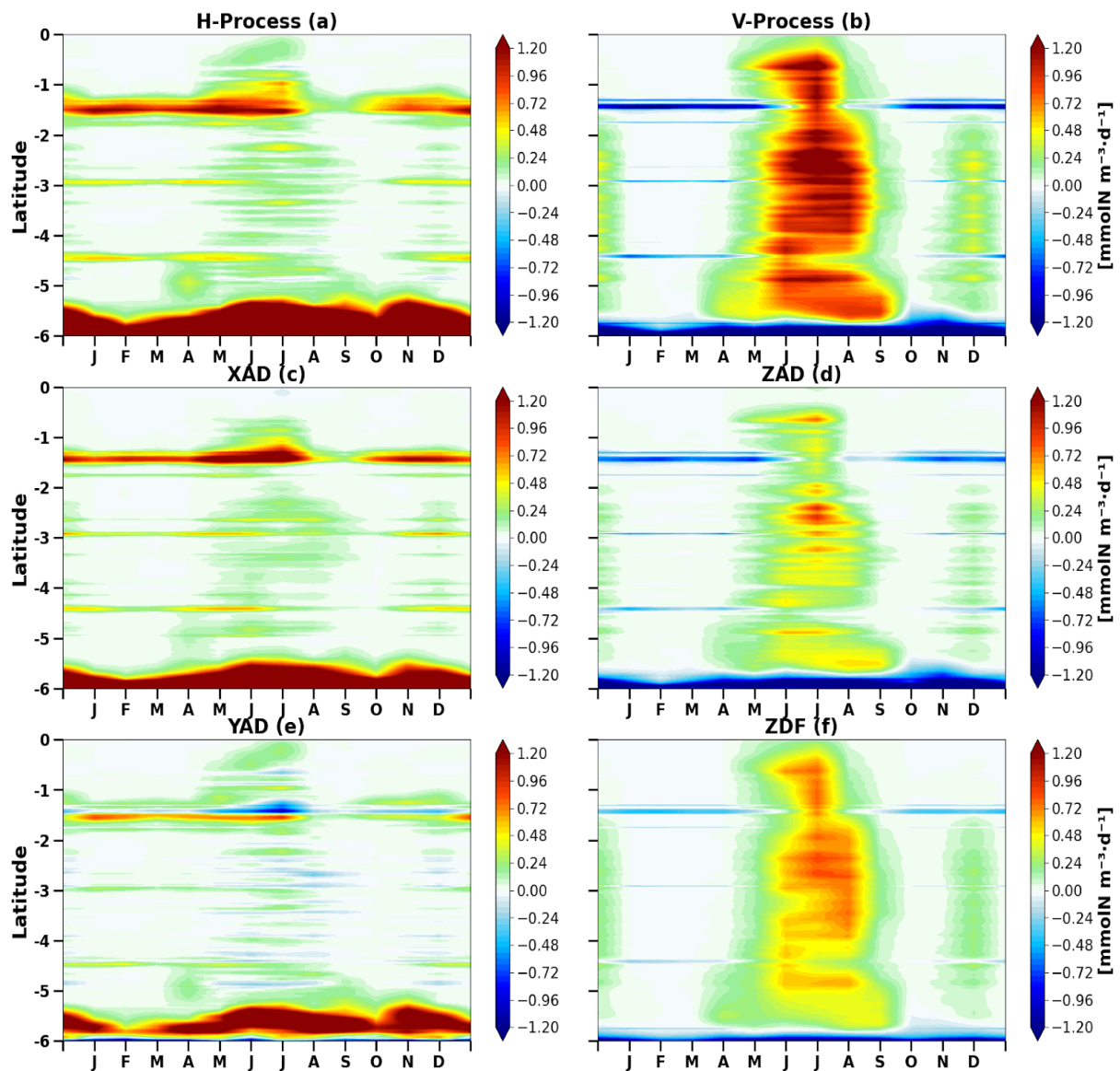


469

470 **Figure 7:** Latitude-time Hovmöller diagram of the model seasonal cycle of Mixed Layer Nitrate (MLN) budget,
 471 a), the rate of the MLN change (b), the physical process contribution (c) and the biological process contribution
 472 (d) along the Gabon-Congo coast. Units are mmolN.m^{-3} and $\text{mmolN.m}^{-3}.\text{d}^{-1}$ for Figure 7a and Figure 7b,c,d,
 473 respectively.

474 In fact, as we can see in the Fig.8, vertical processes (Fig.8b) are the main driver of nitrate supply
 475 during the upwelling between 0°S and 5.5°S with an input magnitude of around $1 \text{ mmol.m}^{-3}.\text{d}^{-1}$ along
 476 the coast while the horizontal processes are the main driver at the vicinity of Congo river mouth (5.5°S
 477 – 6°S) all year long. The latter seems to be dominated by zonal advection (fig.8c) with a very high
 478 nitrate input of more than $1.2 \text{ mmolN.m}^{-3}.\text{d}^{-1}$ nearby 6°S with a northward extension, largest firstly in

479 November-December and secondly in June-July. This is consistent with the seasonal maximum of
 480 Congo River discharge, which suggests a nitrate input through the river plume (Hopkins et al 2013).
 481 North of 6°S, meridional advection (Fig.8e) drives horizontal processes.
 482 The nitrate budget analysis reveals also that vertical processes (Fig.8b) are dominated by vertical
 483 mixing (Fig.8f), while vertical advection has the same seasonality but a smaller contribution (Fig.8d).
 484 Indeed, the nitrate input by the vertical diffusion is about $0.7 \text{ mmolN}\cdot\text{m}^{-3}\cdot\text{d}^{-1}$ but only around 0.5
 485 $\text{mmolN}\cdot\text{m}^{-3}\cdot\text{d}^{-1}$ by vertical advection. Both vertical processes decrease nitrate concentration nearby
 486 6°S, under Congo River plume influence with the dominant zonal advection contribution. Indeed, as
 487 nitrate concentration is greater in the near-surface Congo River plume than in subsurface (between 5 to
 488 10 m, see Fig.3), deeper waters rising at the surface by vertical advection reduce nitrate in the plume
 489 area.

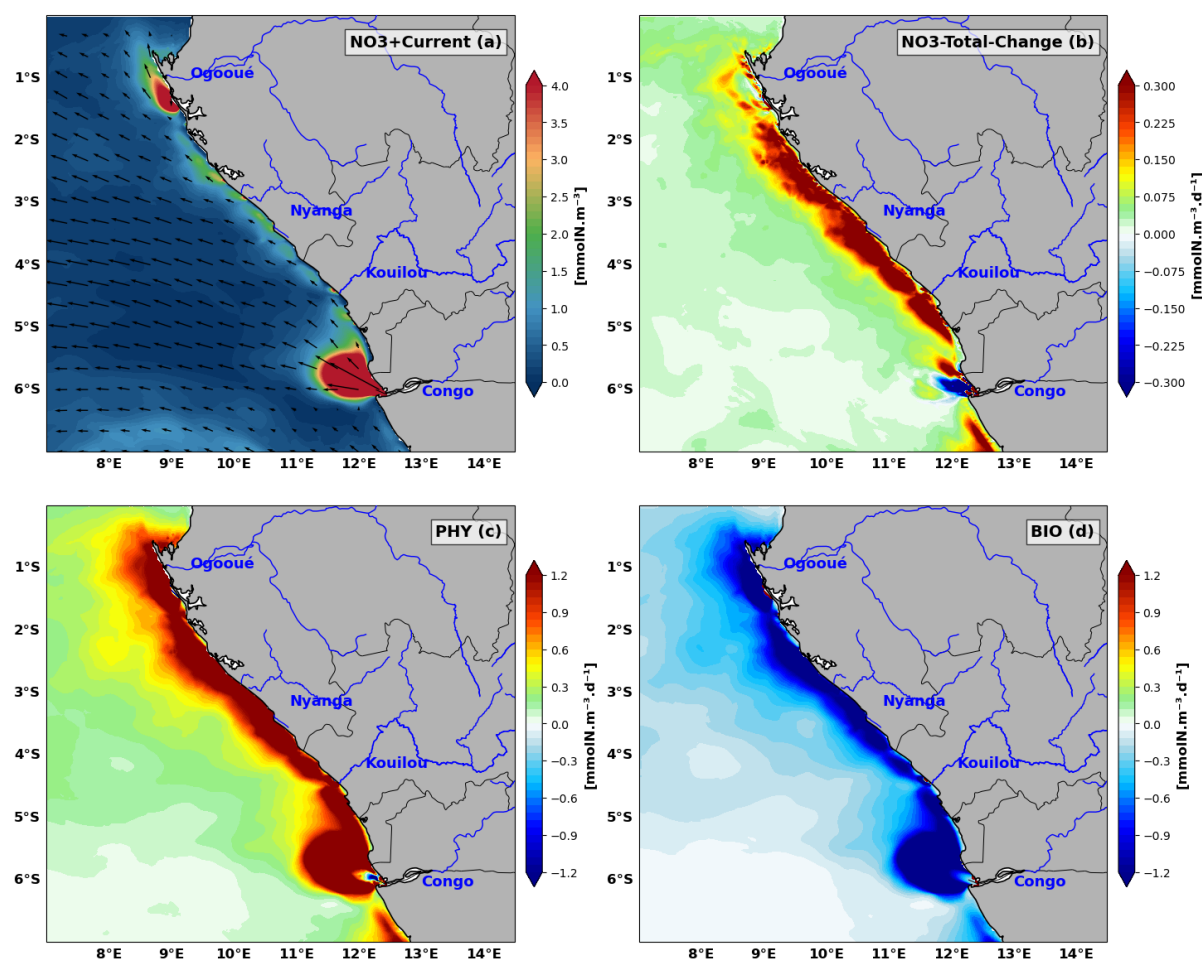


490

491 **Figure 8:** Latitude-time Hovmöller diagram of the model seasonal cycle of horizontal (a) and vertical (b) process
 492 contributions , zonal (c), meridional (e), vertical (d) advectons , vertical diffusion (f) averaged in the mixed
 493 layer along the Gabon-Congo coast. Units are $\text{mmolN}\cdot\text{m}^{-3}\cdot\text{d}^{-1}$.

494 Similarly, vertical mixing of subsurface waters with the plume waters decreases nitrate concentration
 495 at the surface, although the strong haline stratification associated with the Congo River plume limits
 496 this effect.

497 It is important to note that, on the one hand, vertical advection (Fig. 8d) and vertical diffusion (Fig. 8f)
 498 have the same seasonality as SLA (Fig. 4a), in opposite phase, northward of 5.5°S. This suggests that
 499 the upwelling associated with CTWs (negative SLA) induce these vertical processes and therefore
 500 drive the input of nitrate in the northern part of the Gabon-Congo coast. On the other hand, horizontal
 501 advection (both zonal and meridional advections) has the same seasonality as the Congo River
 502 discharge between 5.5°S and 6°S. This suggests that the Congo River supplies nitrate through zonal
 503 advection, near its mouth.



504

505 **Figure 9:** Spatial distribution averaged over the main upwelling period of (a) nitrate, (b) nitrate tendency
 506 contributed by (c) physical processes and (d) biological processes, all averaged in the mixed layer in Austral
 507 winter. The mean current in the mixed layer is superimposed in (a). Nitrate concentration units are $\text{mmolN}\cdot\text{m}^{-3}$
 508 and the tendency terms units are $\text{mmolN}\cdot\text{m}^{-3}\cdot\text{d}^{-1}$.

509 3.2.2 Regional Nitrate Budget Analysis in the main upwelling period: Physical Vs 510 Biological Contributions

511 The regional distribution of nitrate balance terms averaged over the mixed layer for the austral winter
 512 (June-July-August), when upwelling reaches its maximum intensity, is presented in Fig.9. The nitrate
 513 tendency (Fig.9b) shows that during the upwelling period, nitrate input occurs throughout the domain
 514 with values varying between -0.3 to 0.3 $\text{mmolN.m}^{-3}.\text{d}^{-1}$ in the plume zone and 0.2 to 0.56
 515 $\text{mmolN.m}^{-3}.\text{d}^{-1}$ along the coast in the northern part. In the offshore zone, the nitrate tendency is lower,
 516 with a magnitude of around 0.05 $\text{mmolN.m}^{-3}.\text{d}^{-1}$. This distribution of the nitrate tendency shows that
 517 the input of nitrate by physical processes (Fig.9c) is slightly greater than the uptake of nitrate by
 518 biological processes (Fig.9d) throughout the area, explaining the positive nitrate change rate, except at
 519 the Congo River mouth where we have negatives values. Fig.9a shows that nitrate inputs along the
 520 coast are very high close to river mouth and varies a lot along the coast over a width of about 165 km
 521 from the coast. During this main period of upwelling, in general, vertical processes (Fig. 10b) largely
 522 dominate the nitrate supply across the entire continental shelf. A continuous coastal band of strong
 523 enrichment is observed, with values often exceeding 0.513 to 0.677 $\text{mmolN.m}^{-2}.\text{d}^{-1}$. Conversely,
 524 horizontal processes (Fig. 10a) show a more localized and overall lower contribution throughout the
 525 domain, with the notable exception of the Congo and Ogooué River mouth ($\sim 6^\circ\text{S}$ and 1°S
 526 respectively), where a massive positive flux (dark red, > 0.677 $\text{mmolN.m}^{-2}.\text{d}^{-1}$) is observed.
 527 Comparing the spatial structure of the total horizontal process (Fig. 10a) with its individual
 528 components reveals a striking similarity to zonal advection (X_{ad} , Fig. 10c). The X_{ad} signal (Fig. 10c)
 529 almost perfectly reproduces the nitrate patch observed at the Congo mouth, indicating that zonal
 530 transport (east-west) is the main driver of horizontal nitrate injection into the mixed layer, associated
 531 with the offshore extension of the river plume. Although meridional advection (Y_{ad} , Fig. 10e) exhibits
 532 significant dipole structures near the Congo and patches along the coast, its intensity and spatial
 533 pattern provide a less compelling explanation for the overall horizontal process signal. It can therefore
 534 be concluded that zonal advection is the dominant term dictating the distribution of horizontal fluxes
 535 in this region. The study of vertical components shows that the total vertical process (Fig. 10b) results
 536 from two distinct yet complementary mechanisms. Vertical advection (Z_{ad} , Fig. 10d) shows very
 537 intense (> 0.677 $\text{mmolN.m}^{-2}.\text{d}^{-1}$) but highly localized supply along the coastline and capes,
 538 representing the typical signature of coastal upwelling driven by wind and Coastally Trapped Waves
 539 (CTWs). However, vertical diffusion (Z_{df} , Fig. 10f) shows the strongest resemblance to the overall
 540 Vert_Process . It exhibits a broad and homogeneous distribution extending well offshore from the coast,
 541 with sustained values between 0.349 and 0.513 $\text{mmolN.m}^{-2}.\text{d}^{-1}$. Unlike advection, which is highly
 542 segmented, vertical diffusion better explains the spatial continuity of nitrate supply across the shelf.
 543 This suggests that while advection (upwelling) brings nitrate to the base of the mixed layer, turbulent
 544 mixing (diffusion) ensures its effective distribution toward the surface across the entire domain..

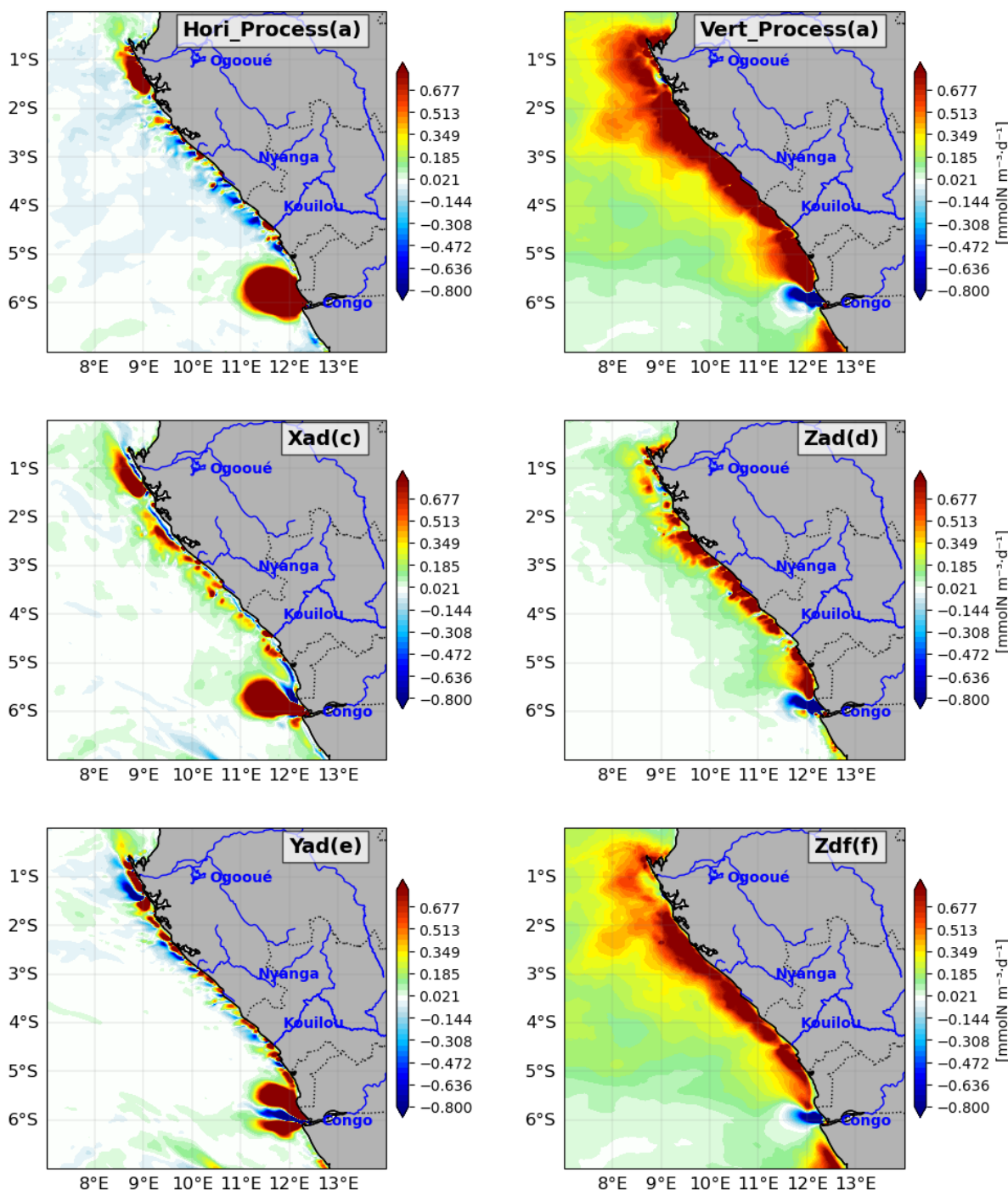
545 3.3 Nitrate budget in the euphotic layer and along the water column

546 Now, in addition to the processes acting in the surface mixed layer, we investigate other processes
547 involved in the nitrate budget below the mixed layer by analysing the nitrate budget in the euphotic
548 layer, generally defined as the zone where light penetration exceeds 1% of the surface light, allowing
549 for the presence of phytoplankton and other photosynthetic organisms. The seasonal variations of
550 thermocline, mixed layer and euphotic layer depths are compared in Fig.11. In Fig.11a, the
551 thermocline (20°C isotherm) variation is very close to the nitracline as suggested by Radenac et al
552 (2020). The mixed layer euphotic layer is very shallow (~ 10 m) throughout the year probably due to
553 the Congo River plume stratification. The euphotic layer extends deeper than the mixed layer, but is
554 generally shallower than the thermocline, except from June to September. The euphotic layer gets
555 thinner during upwelling through the enhancement of CHLa concentration which reduces light
556 penetration (self-shadowing by CHLa). Overall the nitrate tendency (Fig.11b) has the same
557 semi-annual variation in the euphotic layer than in the mixed layer, although more intense in the
558 euphotic layer with a maximum at the bottom of the euphotic layer. In fact, most nitrate input by
559 physical processes (Fig.11c) happens in the mixed layer, where it is almost balanced by biological
560 nitrate uptake (Fig.11d). In contrast, in the euphotic layer below the mixed layer (between 10m and
561 40m depth), biological processes are poorly active and the nitrate variability is almost exclusively
562 induced by physical processes. The mean nitrate input in the euphotic layer is about $0.1 \text{ mmolN.m}^{-3}.\text{d}^{-1}$
563 during the main upwelling period and the maximum input ($0.2 \text{ mmolN.m}^{-3}.\text{d}^{-1}$) occurs in May at the
564 base of the euphotic layer (Fig.11b).

565 In the euphotic layer, biological activity is dominated by photosynthesis which removes nitrate,
566 whereas below the euphotic layer remineralization supplies nitrate with about $0.05 \text{ mmolN.m}^{-3}.\text{d}^{-1}$
567 almost all year long (Fig. 11d).

568 3.3.1 Euphotic Layer Nitrate Budget Analysis: Horizontal Vs Vertical Contributions

569 Fig.12 shows that, even in the euphotic layer, the physical contribution to nitrate supply (Fig.11c) is
570 mostly driven by vertical processes (Fig.12b). However, the large decrease in nitrate (Fig.11b) in
571 October is also caused by horizontal contributions (Fig.12a) in the euphotic layer. Between the surface
572 and 5m depth, horizontal processes dominate nitrate input (Fig.12e). In the euphotic layer below,
573 meridional advection is the main driver of nitrate removal almost year-round, particularly in June and
574 October.

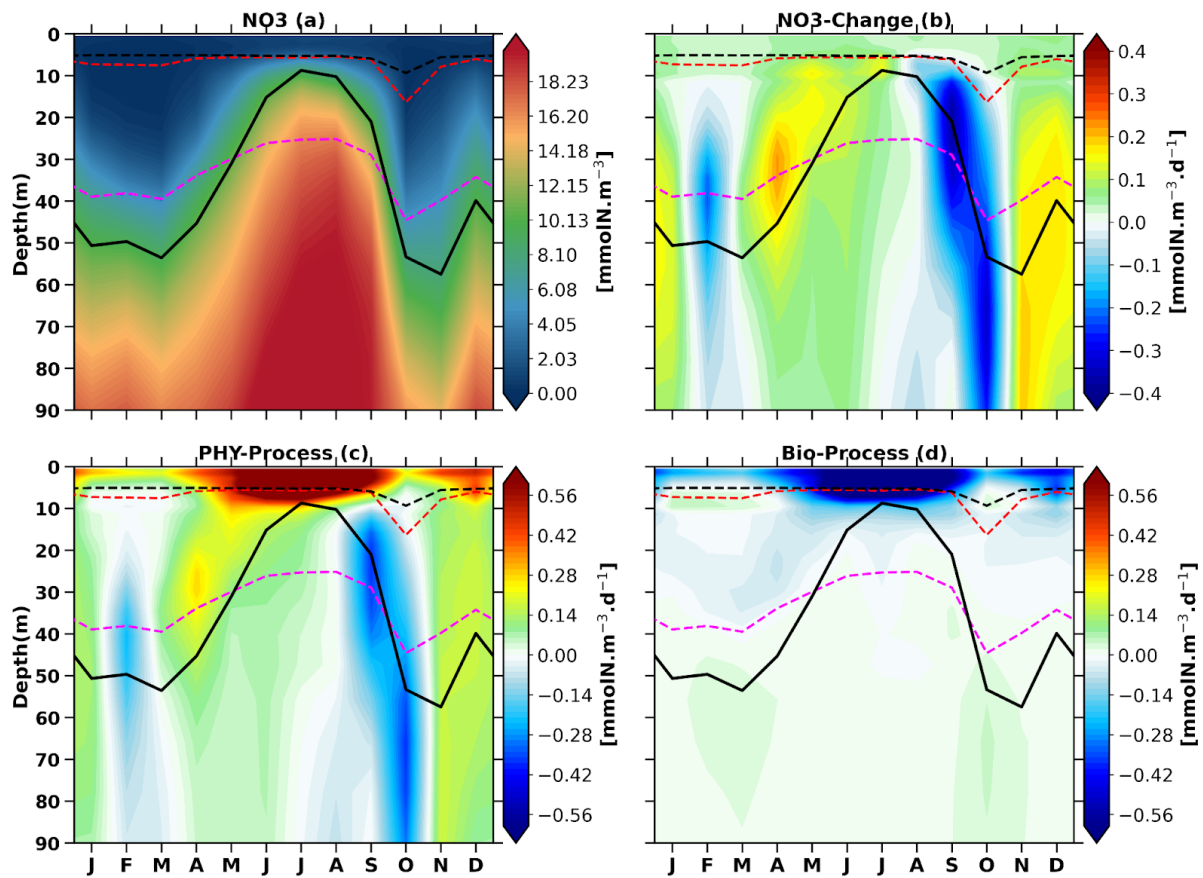


575

576 **Figure 10:** Contribution of (a) the horizontal processes, including (c) zonal advection and (e) meridional
 577 advection, and (b) vertical processes, including (d) vertical advection and (f) vertical diffusion, to the nitrate
 578 budget averaged in the mixed layer during the austral winter. Units are $\text{mmolN} \cdot \text{m}^{-3} \cdot \text{d}^{-1}$.

579 Zonal advection (Fig.12c) supplies nitrate in the euphotic layer, with a maximum above the mixed
 580 layer depth, throughout the year. This nitrate input is more than compensated by nitrate lost by
 581 meridional contribution, below the upper 5 m (Fig.12e), except in June, July and August. Vertical
 582 advection (Fig.12d) is the dominant vertical process (Fig.12b) in the nitrate budget. Below 30 m depth,
 583 it has a semi-annual cycle characteristic of upwelling and downwelling CTWs propagation, associated

584 with nitrate increase when the thermocline shallows and nitrate decrease when the thermocline
 585 deepens, with the maximum and minimum values around the thermocline depth. Moreover, vertical
 586 advection supplies more nitrate in the mixed layer than in the euphotic layer below during the main
 587 upwelling period (June, July and August), but rather the opposite during the second upwelling period
 588 (December). Between the mixed layer depth and the euphotic layer depth, vertical diffusion (Fig.12f)
 589 tends to partially compensate for the effects of vertical advection on nitrate. However, in the mixed
 590 layer it mostly supplies nitrate, particularly during the upwelling seasons.



591

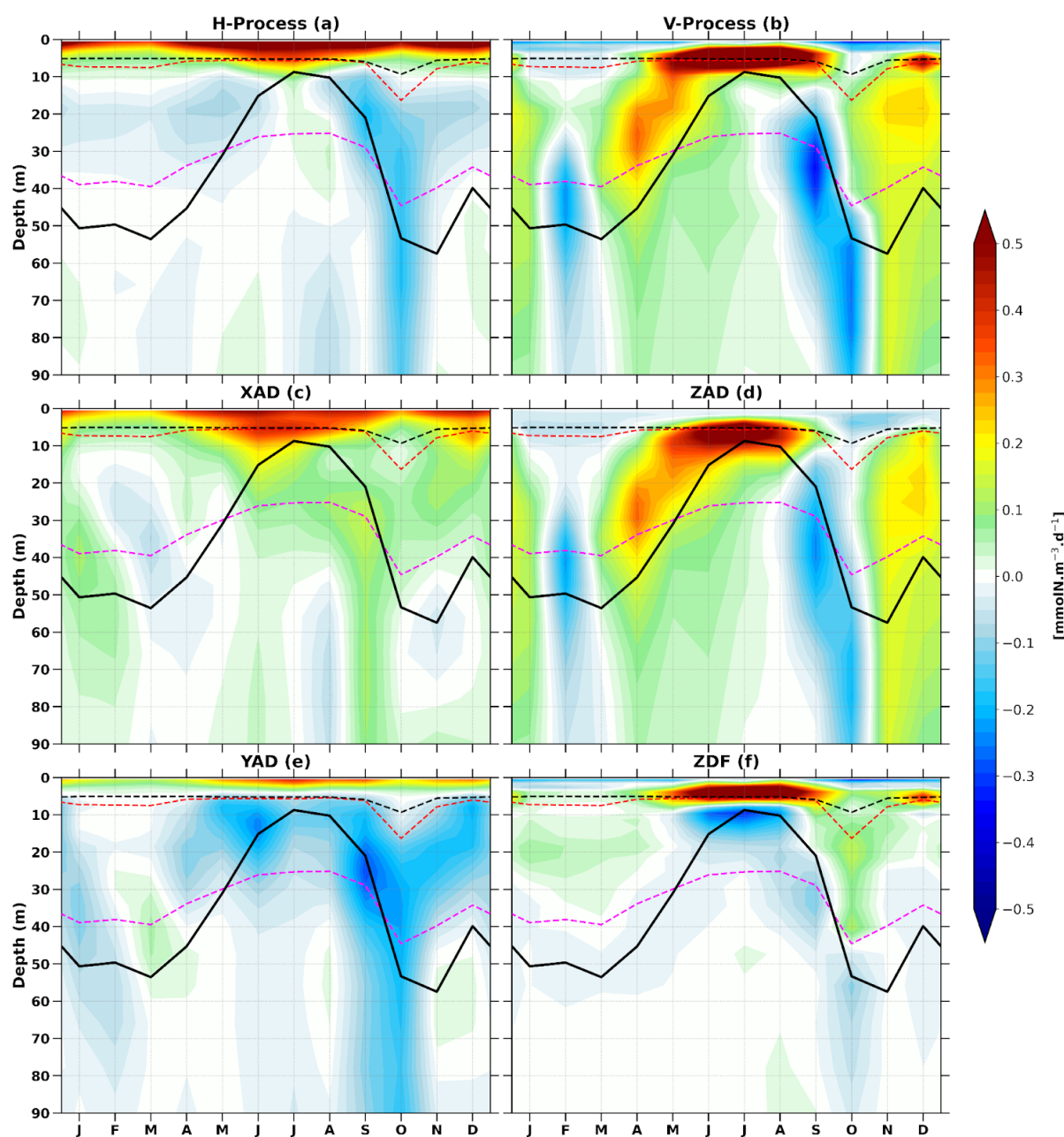
592 **Figure 11:** Depth-time Hovmöller diagram of the seasonal cycle of the nitrate budget averaged within the
 593 Gabon-Congo coastal box (0°S – 6°S , 1° wide coastal band, as shown in Fig. 1). (a) Nitrate concentration
 594 (mmolN.m^{-3}), (b) nitrate rate of change, (c) physical process contribution, and (d) biological process
 595 contribution ($\text{mmolN.m}^{-3}.\text{d}^{-1}$). The black solid line represents the thermocline (20°C isotherm), while dashed
 596 magenta, red and black lines indicate the euphotic, isothermal and mixed layer depths, respectively.

597 3.3.2 Nitrate budget analysis: advection components analysis

598 As nitrate advection depends on velocity and on the nitrate gradient, we now evaluate the individual
 599 contributions of seasonal variations in velocity and nitrate gradient, as well as their combined effect, to
 600 the seasonal variations of nitrate advection (see section 2.3, equation 4).

601 3.3.2.1 Nitrate budget analysis: horizontal advection

602 Fig.13 allows to visually compare the depth-time structure of the zonal nitrate advection (Fig.13a)
 603 with that of its different components, while correlation r is used to quantify the comparison.

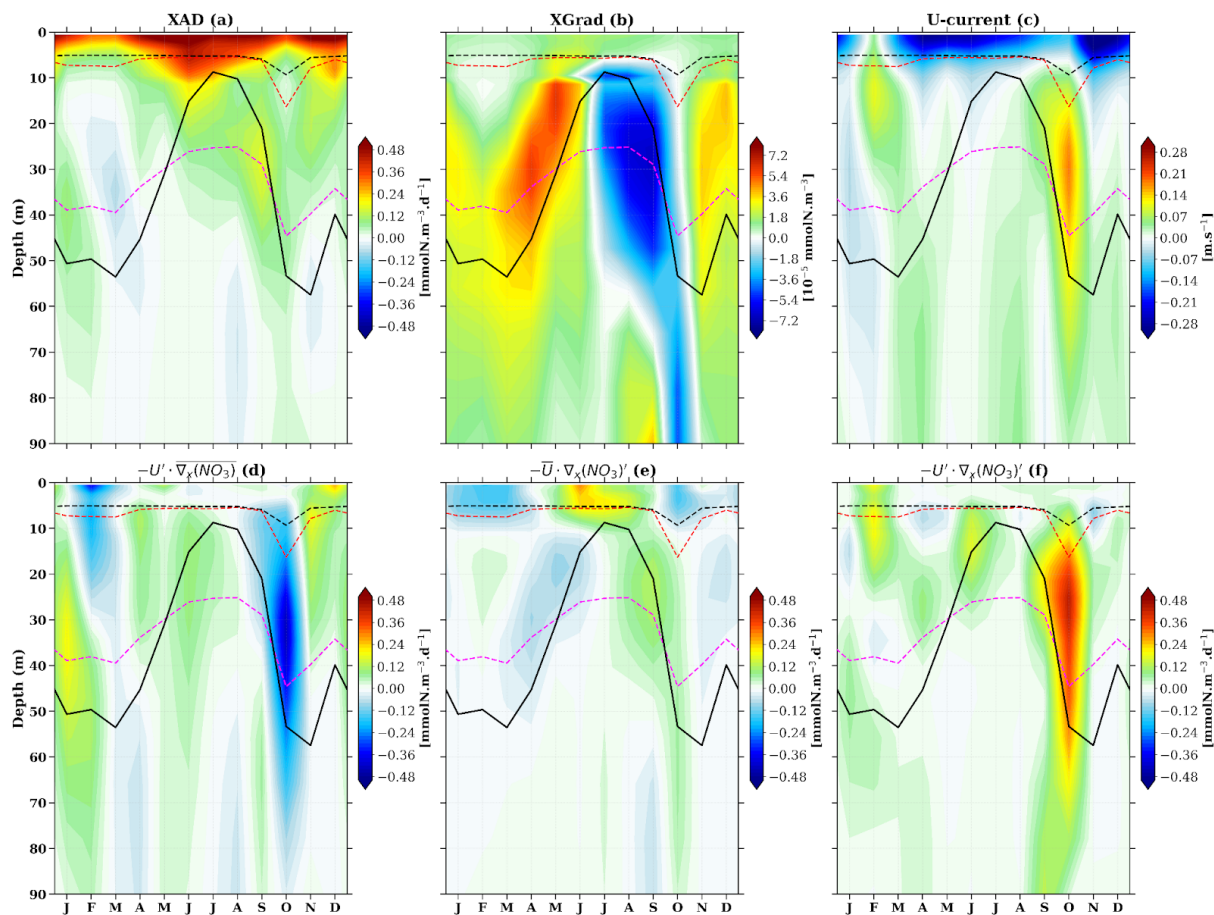


604

605 **Figure 12:** Depth-time Hovmöller diagram of the model seasonal cycle of contributions to the nitrate budget of
 606 horizontal and vertical processes (a and b respectively), zonal, meridional, vertical advections (c, e and d
 607 respectively), vertical diffusion (f) along the Gabon-Congo coast (0°S-6°S and 1° width to the coast). Units are
 608 mmolN.m^{-3} for all of the plots. The black solid line represents the thermocline (20°C isotherm), while dashed
 609 magenta, red and black lines indicate the euphotic, isothermal and mixed layer depths, respectively.

610 The seasonal cycle of zonal nitrate advection in the 0-100 m water column (Fig. 13a) is controlled first
 611 by the term $\overline{u \cdot \nabla x(NO_3)}$ (Fig.13e, $r=0,77$, $p<0,05$), i.e. the annual mean zonal current multiplied by
 612 the seasonal variations of the nitrate zonal gradient, second by the term $u \cdot \overline{\nabla x(NO_3)}$, (Fig.13d, $r=0,49$,
 613 $p<0,05$), i.e. the seasonal variations of the zonal current multiplied by the annual mean nitrate zonal
 614 gradient, and third (and much less) by the term. The third component, which represents the

615 simultaneous variation in zonal current and nitrate gradient $u' \cdot \nabla_x(NO_3)'$, (Fig.13f, $r=-0,15$, $p<0.05$),
 616 i.e. the product of seasonal variations of both the zonal current and the nitrate zonal gradient. The
 617 seasonality of the zonal current (Fig. 13c) is influenced by the seasonal cycle of the South Equatorial
 618 Undercurrent (SEUC), with maximum values in September-October and February-March (Dorothee et
 619 al, 2004) in this zone ($0^\circ\text{S}-6^\circ\text{S}$, 1° from the coast). Thus we can conclude that the SEUC plays a key
 620 role in the nitrate balance in the Gabon-Congo system by bringing nitrate in February-March and in
 621 September-October to the euphotic layer.



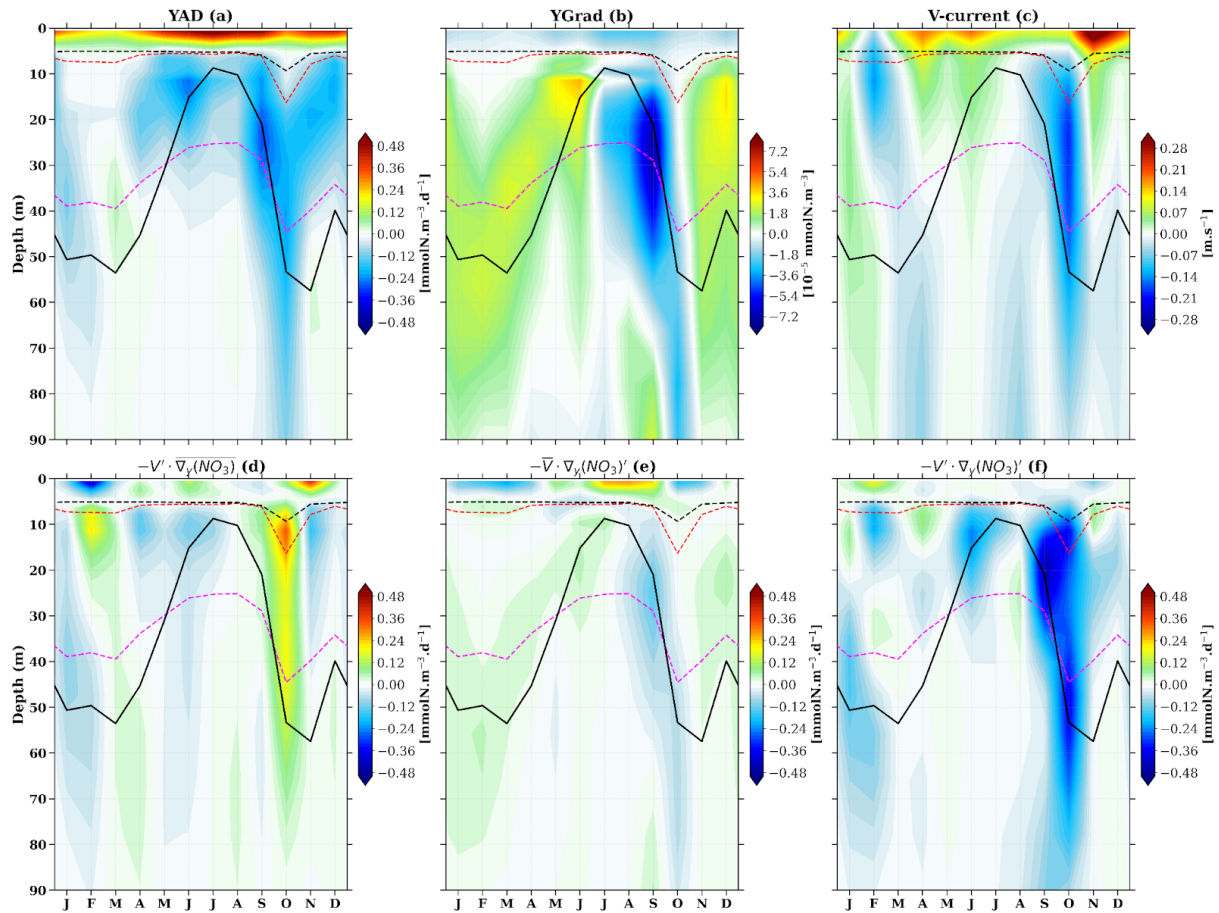
622 **Figure 13:** Depth-time Hovmöller diagram of the model seasonal cycle of nitrate advection (a), nitrate gradient
 624 (b), zonal current (c), zonal current variation times mean nitrate gradient (d), gradient variation times mean
 625 current (e) and gradient variation times zonal current variation (f), all along the zonal axis in the Gabon-Congo
 626 coastal box of Fig. 1. Units are milli mol per cubic meter per day for all of the plots except (b) (milli mol per
 627 cubic meter) and (c) (meter per second). The black solid line represents the thermocline (20°C isotherm), while
 628 dashed magenta, red and black lines indicate the euphotic, isothermal and mixed layer depths, respectively.

629 In the euphotic layer, we see that, as for the meridional nitrate advection, the meridional current
 630 (Fig.14c) looking at the shape seems to be the main factor in the vertical and temporal variation shape
 631 of the meridional nitrate advection (Fig.14a). The Angola current (AC), is the factor which modulates
 632 nitrate lost by meridional nitrate advection throughout the year, with maximum loss in
 633 September-October and June-July, in and below the euphotic layer, except in the first 5 m-depth.

634 Our analysis in this section reveals that the simultaneous variation in both the meridional current and
 635 the gradient ($v' \cdot \nabla y(NO_3)$), Fig.14f) exhibits the highest correlation ($r=0.527$, $p<0.05$) with meridional
 636 nitrate advection, thus explaining the major changes in advection. This result highlights the significant
 637 impact of the concurrent variability of both meridional current and gradient on meridional nitrate
 638 advection in the euphotic layer. In contrast, gradient variation ($\overline{v' \cdot \nabla y(NO_3)}$), Fig.14e) is poorly
 639 correlated ($r=0.97$, $p<0.05$) with meridional nitrate advection. The very low positive correlation with
 640 total meridional advection (a) indicates this term, representing the effect of a mean meridional current
 641 acting on a fluctuating nitrate gradient. This suggests that either the mean meridional current is weak,
 642 or its interaction with the fluctuating gradient does not lead to significant changes in overall advection.
 643 The variation in the meridional current ($v' \cdot \overline{\nabla y(NO_3)}$), Fig.14d) shows the lowest correlation ($r=0.287$,
 644 $p<0.05$). This low, negative correlation with total meridional advection (Fig.14a) indicates that this
 645 term, representing the effect of fluctuating meridional currents on a relatively stable mean nitrate
 646 gradient, is not a dominant driver of the overall meridional nitrate advection. In fact, a negative
 647 correlation suggests it might weakly oppose the main advection pattern or have an inverse relationship.
 648 This implies that the mean gradient is either small or the meridional current variations are not aligned
 649 to produce significant advection changes via this mechanism.

650 3.3.2.2 Nitrate budget analysis: vertical processes

651 Our analysis reveals that within the euphotic layer, the variation in the vertical gradient $\overline{w' \cdot \nabla z(NO_3)}$,
 652 Fig.15e) appears to better explain the variation in vertical nitrate advection (Fig.15a), showing a
 653 correlation of $r=0.79$ ($p<0.05$). In contrast, vertical velocity variation ($w' \cdot \overline{\nabla z(NO_3)}$), Fig.15d) plays a
 654 secondary role, with a correlation of approximately 0.646 ($p<0.05$) with vertical nitrate advection.
 655 Looking now at the vertical nitrate advection, we can see strong similarities in the vertical and
 656 temporal variation structure between vertical advection seasonality (Fig.15a), vertical nitrate gradient
 657 seasonality (Fig.15b) and vertical velocity seasonality (Fig.15c), both three are very strong in the
 658 euphotic layer. We can also see in the semi-annual vertical velocity that from April to August and
 659 November-December, vertical velocities are upward corresponding to negative values of SLA (Fig.4a,
 660 4b), lowest SST (Fig.4c, 4d) values and highest nitrate concentration (Fig.4e, 4f). From January to
 661 March and September-October, vertical velocities are downward corresponding to positive values of
 662 SLA (Fig.4a, 4b), highest SST (Fig.4c, 4d) values and lowest nitrate concentration (Fig.4e, 4f). This
 663 later observation confirms that CTWs propagating from April to August and November-December are
 664 associated with upwelling. In contrast, CTWs propagating from January to March and
 665 September-October are associated with downwelling. Note that similar results were found by Ngakala
 666 et al. (2025) for the seasonal heat budget in the Gabon-Congo upwelling (from 4°S-6°S and 1° width
 667 to the coast) and also further south in the Angolan upwelling by Korner et al. (2024).



668

669 **Figure 14:** Depth-time Hovmöller diagram of the model seasonal cycle of nitrate advection (a), nitrate gradient
 670 (b), meridional current (c), meridional current variation times mean nitrate gradient (d), gradient variation times
 671 mean meridional current (e) and gradient variation times current variation (f), all along the meridional axis in the
 672 Gabon-Congo coastal box of Fig. 1b. Units are milli mol per cubic meter per day for all of the plots except (b)
 673 (milli mol per cubic meter) and (c) (meter per second). The black solid line represents the thermocline (20°C
 674 isotherm), while dashed magenta, red and black lines indicate the euphotic, isothermal and mixed layer depths,
 675 respectively.

676 However, if we average in the first hundred meters, vertical velocity variation has the highest
 677 correlation of 0.831 ($p < 0.05$) with vertical advection, whereas vertical gradient variation has only 0.63
 678 ($p < 0.05$) of correlation with vertical advection. The third component ($w' \cdot \nabla_z(NO_3)'$, Fig.15f) has a
 679 lower negative correlation -0.062 ($p < 0.05$) with vertical advection. During the upwelling period, the
 680 variation in vertical gradient (Fig.15e) at the base of the mixed layer has a much greater influence on
 681 nitrate supply than the variation in vertical velocity (Fig.15e). Another observation is that in the same
 682 main upwelling period there is a lag between maximum vertical current which happens in May and the
 683 maximum vertical gradient indicated by the shallowest thermocline in July. This lag results in a
 684 highest input of nitrate by vertical advection (Fig.15a) in the mixed layer in June. It can be seen that
 685 the nitrate output by vertical advection during the downwelling period is mostly induced by the

686 vertical nitrate gradient in the mixed layer whereas deeper in the euphotic layer these losses are
687 induced by vertical downward velocities induced by downwelling CTWs propagation.

688 **4 Discussion**

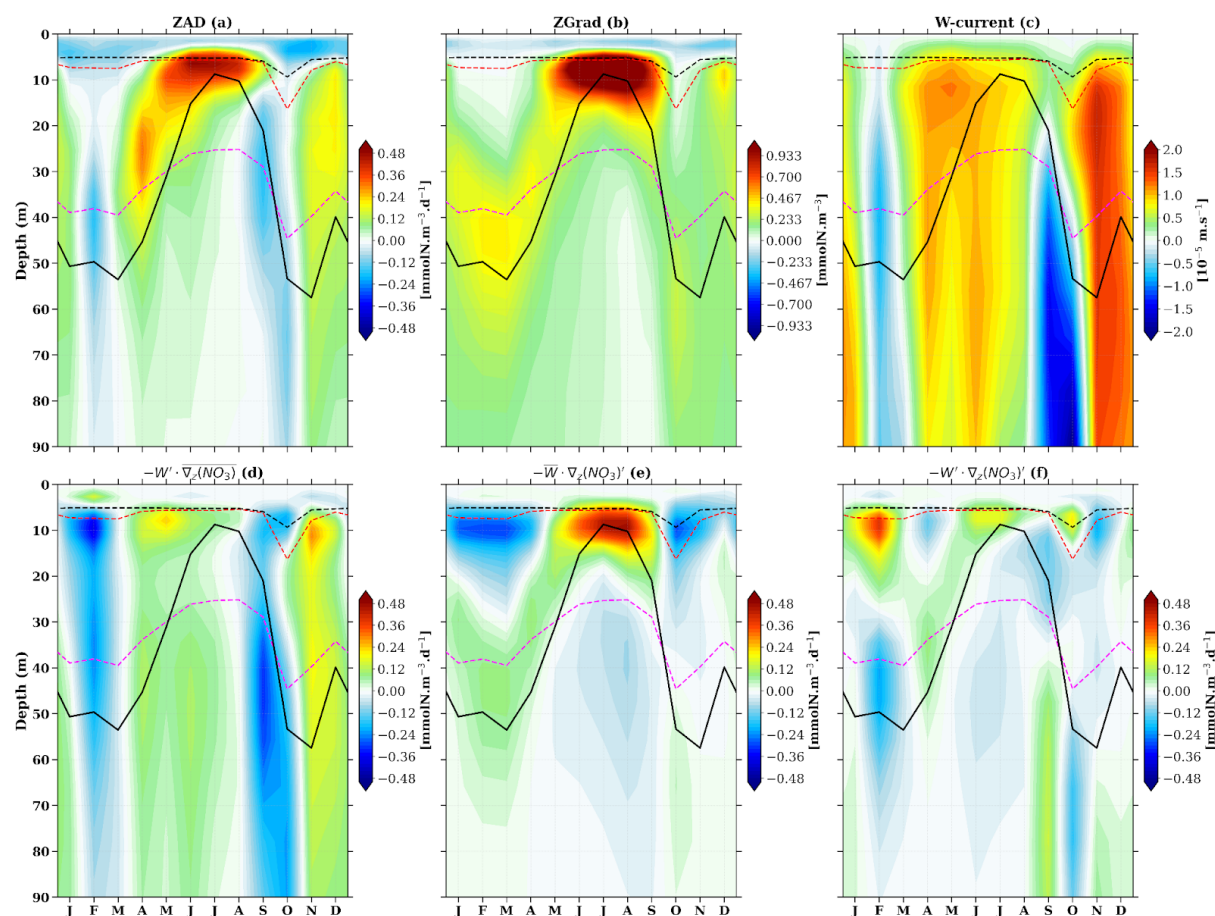
689 In this section, we discuss our results: the model-data comparison, the influence of the mixed layer
690 criteria, the main nitrate budget drivers in the Gabon-Congo upwelling system compared to the other
691 tropical Atlantic upwelling systems. Finally, we will explore the factors governing seasonal
692 productivity in the Gabon-Congo upwelling system, integrating our understanding of physical forcing
693 and nutrient availability to characterize its biological response. Through this comprehensive
694 discussion, we aim to provide a nuanced understanding of the oceanographic processes at play in the
695 coastal Congo region and the capabilities and limitations of our modeling approach.

696 Throughout this work, we have shown that our model reasonably reproduces the observations in terms
697 of temperature, nitrate, CHLa, SLA and surface currents, although there are a few differences that we
698 will discuss in this section. First of all, we saw that temperature in our model is warmer than observed
699 by around 1°C in regional distribution (Fig. 2a,b) as well as in seasonal cycles (Fig. 4c,d). This is a
700 common bias in ocean and climate models in the Eastern tropical Atlantic (Richter, 2015; Zuidema et
701 al., 2016; Voltaire et al., 2019). Indeed, several studies suggest that this warm bias is multicausal.
702 While it is partly attributed to models' deficiency in simulating low-level clouds, resulting in
703 overestimation of shortwave radiation (Xu et al., 2014), other factors play a critical role. These include
704 errors in atmospheric forcing, specifically the misrepresentation of the coastal low-level jet and wind
705 stress, which can weaken coastal upwelling (Cabos et al., 2017; Voltaire et al., 2019). Furthermore,
706 complex air-sea feedback mechanisms (Koseki et al., 2018) and difficulties in simulating the vertical
707 thermocline structure in the region (Koubanova et al., 2018) are also shared challenges that contribute
708 to this persistent modeling bias.

709

710

711



712

713 **Figure 15:** Depth-time Hovmöller diagram of the model seasonal cycle of nitrate advection (a), nitrate gradient
 714 (b), vertical current (c), vertical current variation times mean nitrate gradient (d), gradient variation times mean
 715 vertical current (e) and gradient variation times current variation (f), all along the vertical axis in the
 716 Gabon-Congo coastal box of Fig. 1b. Units are milli mol per cubic meter per day for all of the plots except (b)
 717 (milli mol per cubic meter) and (c) (meter per second). The black solid line represents the thermocline (20°C
 718 isotherm), while dashed magenta, red and black lines indicate the euphotic, isothermal and mixed layer depths,
 719 respectively.

720 With regard to nitrate concentrations, the regional distribution shows that north of the mouth of the
 721 Congo River and near the coast, the model agrees well with the CARS climatology (Fig. 2c,d).
 722 However, offshore and south of the mouth of the Congo River, the model underestimates nitrate
 723 concentrations. In the seasonal cycle, we see that the model captures the seasonal variability, but
 724 underestimates the amplitude compared to the data. These biases may be explained by the temporal
 725 coverage of the CARS climatology, which covers a long period (from 1940 to 2011) of data
 726 (Bachelery et al., 2016) compared to our model which covers only one year (2011). Another bias may
 727 be the lack of data in CARS, in our study area.. The differences in the surface CHLa concentration
 728 between the model and the satellite observations may be associated with a lack of data for the ocean
 729 colour satellite observations, particularly in August, due to the cloud cover which induces atmospheric
 730 contaminations (Hardman-Mountford and McGlade., 2002; Estival et al., 2013) of the satellite signal,

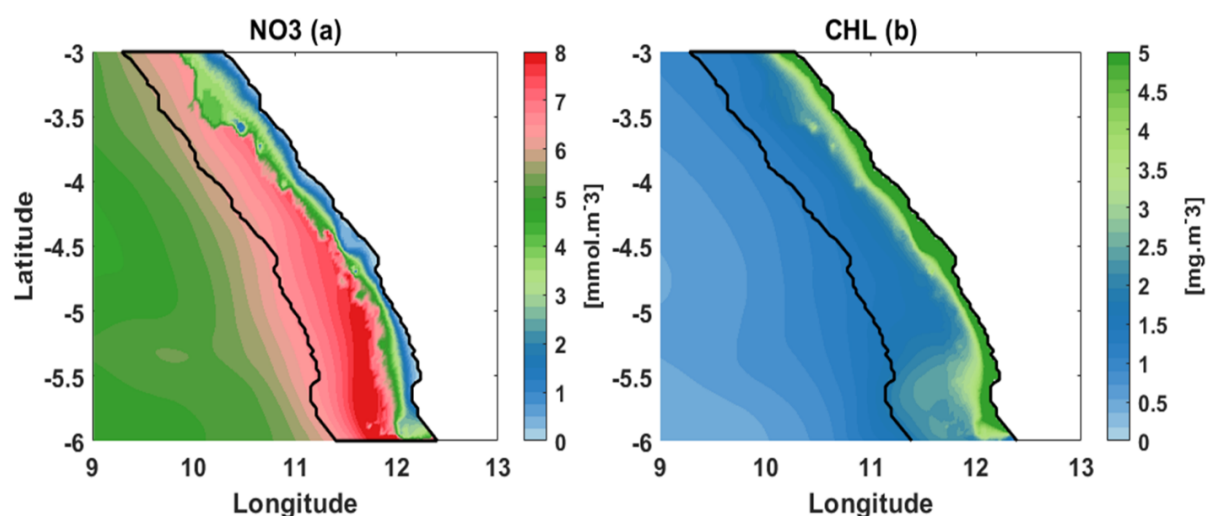
731 resulting in a lack of CHLa signal (Nieto et al., 2016). The biases in the surface currents between the
732 model and the observations are mainly due to the underestimation of the currents in the OSCAR
733 product near the coastal zone (Sikhakolli et al., 2013), especially in our studied area where very few
734 data are available. Despite these results discussed earlier in this paper, we have to keep in mind that
735 there are also some limitations in our simulation. For example, the model has difficulties reproducing
736 the seasonal cycle of CHLa concentration, in particular the first CHLa blooms occurring in
737 February-March, highlighted by the MODIS ocean colour satellite data. This might be due to the
738 CHLa concentration of the Congo river in our model. Indeed, we take into account the nutrients and
739 dissolved organic matter discharges of the river but not the CHLa concentrations (information not
740 available in the HYBAM database). We can also observe a minimal or slightly reduced concentration
741 of CHLa around the mouth of the Congo River in our model (Fig. 2e). This is explained by the very
742 high speed (greater than 2 m/s) of the Congo River current at its mouth in our model. This has resulted
743 in the transport of CHLa produced by phytoplankton photosynthesis away from the mouth of the
744 Congo River.

745 Our analysis shows that, in the Gabon-Congo upwelling system, the nitrate budget in the mixed layer
746 is dominated by physical processes during the upwelling period (Fig. 7c), particularly vertical
747 diffusion (Fig. 8f), while zonal advection and vertical mixing play a secondary role. In agreement to
748 these latter results, Ngakala et al. (2025) using a high resolution simulation ($1/36^\circ$) of NEMO in the
749 Gabon-Congo upwelling, have shown through a mixed layer heat budget, that vertical diffusion was
750 the main contributor of cooling during upwelling period in the mixed layer. They found that the
751 vertical advection has a secondary role in cooling of the mixed layer. They state that, if defining
752 instead the mixed layer depth with the Boyer-Montégut criterion, then vertical advection would play a
753 greater role than vertical diffusion. Thus, as mentioned in our study and in agreement with Ngakala et
754 al. (2025), the relative contributions of vertical advection and diffusion depend on the definition of the
755 mixed layer depth.

756 Our analysis reveals that the seasonal variability of CHLa in our region is driven by the seasonal
757 concentration of nitrate, as in other tropical Atlantic upwelling systems (Radenac et al., 2020).
758 However different processes drive the seasonal cycle of nitrate and CHLa in the different tropical
759 Atlantic upwelling systems. In the Equatorial Atlantic upwelling system, the seasonal cycle of nitrate
760 and CHLa are driven by the wind stress and wind stress curl (Caniaux et al., 2011, Radenac et al.,
761 2020). In the Tropical Angola Upwelling system, the main driver of these seasonal cycle are the CTWs
762 as in our area with a main peak in austral winter (May-July) and a second peak in December-January.
763 However vertical mixing plays also a key role in the Tropical Angola Upwelling system (Awo et al.,
764 2022; Ostrowski et al., 2009; Körner et al., 2023) due to onshore propagating internal tide waves
765 interacting with sloping topography (Brandt et al., 2023). In the upwelling systems of the equatorial
766 Atlantic and tropical Angola, vertical mixing is the main driver of nitrate input to the mixed layer. This
767 is due to local mechanisms that occur in these areas (local forcing), such as the intensification of the

768 vertical shear stress between the South Equatorial Current (SEC) and the Equatorial Undercurrent
769 (EUC) at the equator (Jouanno., 2010, Radenac et al., 2020) and the dissipation of internal tide that
770 interact with the continental shelf and produce turbulent mixing at the Angolan coast (Körner et al.,
771 2023, Zeng et al., 2021, Brandt et al., 2023). In the Gabon-Congo system, we can suggest that the
772 strong stratification induced by the discharge of the Congo River, which is the second largest river in
773 the world, contributes to thinning the mixed layer, limiting the effect of mixing very close to the
774 surface (Dossa et al., 2019).

775 In the euphotic layer and below, the nitrate budget is almostly dictated by physical processes, which
776 are mainly modulated by currents that transport water of different properties. We noted that vertical
777 and zonal advectons were the drivers of nitrate input in the upwelling period, while vertical mixing
778 and meridional advection were the drivers of nitrate losses in the lower part of the euphotic layer (just
779 below the mixed layer depth) in this period. However, during the downwelling period, vertical mixing
780 mostly brings nitrate to the lower part of the euphotic layer, while vertical and meridional advection
781 always remove nitrate. Meridional advection is therefore the main factor in nitrate loss in the euphotic
782 layer all year long. This is consistent with the warming effect of meridional advection shown by
783 Körner et al. (2023) in the Angolan upwelling. Radenac et al (2020) showed that in the equatorial
784 euphotic layer, zonal advection by the EUC current was the main driver of nitrate losses, which may
785 explain our previous results since the southward Angola current dominating the ocean circulation in
786 the Congo-Angola zone is fed by the EUC current. Indeed, the EUC, whose source waters come from
787 the oligotrophic layers of the subtropical South Atlantic, has relatively low nitrate concentrations
788 compared to neighbouring waters (Schott et al., 1998; Johns et al., 2014; Tuchen et al., 2022a). These
789 low nitrate waters are brought to the Congo-Angola system by the Angola Current (AC) (Fig.16),
790 reducing nitrate concentration in the euphotic layer. At the same time, the AC brings CHLa into the
791 euphotic layer by meridional advection, as the EUC has relatively high CHLa concentrations (Radenac
792 et al., 2020). This low nitrate / high CHLa signature of the AC can be seen in the first hundred metres
793 and in particular at the base of the euphotic layer along the Gabon-Congo coast (Fig.A1c), where the
794 AC flows (Kopte et al, 2017). Further analyses show that the coastal CHLa maximum occurs from
795 May to September with a peak in August, which is consistent with the seasonal cycle of the CHLa
796 concentration in the EUC (Radenac et al, 2020; Brandt et al, 2023). The simultaneous variation in
797 current and gradient appears to be the main factor contributing to variations in the meridional
798 advection and nitrate removal, mainly between July and October. Over the same period, we observe a
799 sign change of the meridional nitrate gradient (Fig.14b), which is generally positive (indicating that
800 under the mixed layer, waters to the south of the coastal box (0°N–6°S, 1° width from the coast; see
801 Fig. 1b) are less nitrate-rich than waters to the north) under the mixed layer from January to June.



802

803 **Figure 16:** Regional distribution of mean annual nitrate and CHLa concentration (a, b respectively) averaged on
 804 the 0-100 m layer along the Gabon-Congo upwelling area, black line represents different boundaries of our
 805 Coastal box with a width of 1° of longitude relative to the coast.

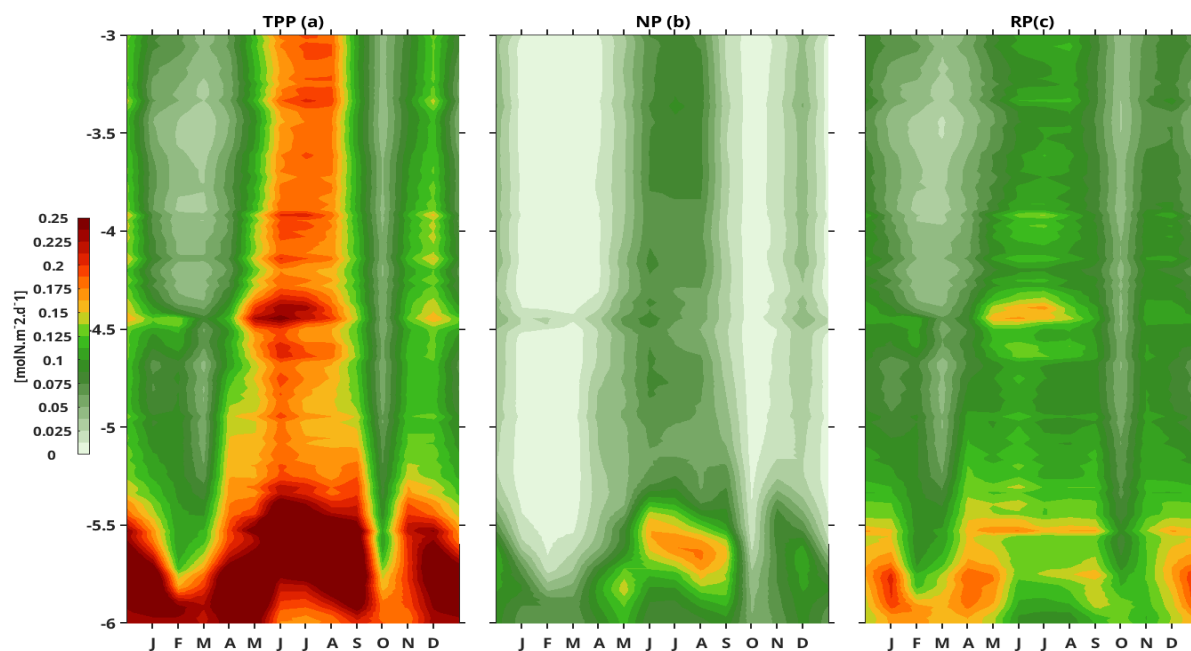
806 This observation suggests that for the period from September to October, waters in the southern part of
 807 the box are now richer in nitrate than waters in the northern part of the box under the mixed layer.
 808 Beyond horizontal transport, this frontogenesis is also driven by the meridional gradient of vertical
 809 motion ($\partial w/\partial y$). A stronger upward vertical velocity in the southern section (near 6°S) compared to the
 810 north leads to a higher vertical nitrate supply in the south, establishing the negative meridional nitrate
 811 gradient observed in Fig. 14b. This highlights the important role of vertical processes in the regional
 812 enrichment, as also emphasized by Nubi et al. (2016) for the equatorial band. This also reflects the
 813 passage of low-nitrate waters from the EUC via the Angola Current to the Gabon-Congo coast.
 814 However, we find that zonal advection brings nitrate in the euphotic layer and its decomposition has
 815 shown that its variation is mostly influenced by zonal nitrate gradient variation, with a secondary
 816 contribution of zonal current variation. This zonal current variation is seen to remove nitrate in the
 817 euphotic layer during February-March and July-October. We can also see that in these periods the
 818 zonal current flows toward the coast, which suggests that it brings low nitrate water from offshore
 819 toward the coast. This seasonally eastward current is consistent with the seasonal cycle of SEUC
 820 (Siegfried et al., 2019; Assene et al., 2022). Besides this, we can also see that there is a sign change of
 821 the zonal nitrate gradient (Fig.13b) which occurs simultaneously with the sign change of the
 822 meridional nitrate gradient (Fig.14b) suggesting that this inversion in zonal nitrate gradient is due to
 823 Angola Current water at the coast. In fact, this later result highlights that the Angolan Current waters
 824 flowing along the coast are less rich in nitrate than the water brought from offshore toward the coast by
 825 the SEUC. As nitrate concentration in the coast is lower, SEUC waters act to increase nitrate
 826 concentration in our coastal box, through zonal advection in the euphotic layer from April to
 827 December. The CHLa budget analysis (Appendix A, Fig. A1) shows that the SEUC brings through
 828 zonal advection low CHLa water at the coast thereby reducing the nitrate input during the

829 downwelling period. In the nitrate budget we saw that the main driver of nitrate input was vertical
830 advection associated with CTWs. Körner et al. (2024) have shown, using satellite and mooring data,
831 that CTWs detected in the SLA are of the low vertical mode, while the movement of the isopycnals is
832 rather consistent with the vertical velocity structure of higher modes. This explains why isopycnals
833 reach their seasonal minimum/maximum depth (in phase with the nitracline) after the minimum in
834 SLA (Körner et al, 2024). The spatial distribution of mean annual nitrate and CHLa concentrations
835 (Fig. 16a, b) provides clear evidence of the influence of the Angola Current (AC) on the coastal
836 biogeochemistry of the Gabon-Congo system. Physically, the AC is a southward-flowing coastal
837 current that advects warm, equatorial-origin waters along the shelf. Biogeochemically, our model
838 results (Fig. 16a) show that while the broader coastal box is enriched in nutrients due to upwelling and
839 riverine inputs, there is a distinct relative decrease in nitrate concentrations strictly along the shoreline,
840 particularly south of 5°S. In this narrow coastal band, NO_3 values are lower than those found in the core
841 of the upwelling plume located slightly further offshore. Conversely, the chlorophyll-a map (Fig. 16b)
842 reveals a robust coastal belt with maximum concentrations exceeding $4.5 \text{ mg}\cdot\text{m}^{-3}$ right at the coast.
843 This low-nitrate / high-CHLa inverse relationship at the immediate coastline is consistent with the
844 known characteristics of the Angola Current. Indeed, the AC transports mature waters originating from
845 the Equatorial Undercurrent (EUC).

846 We assessed the variability of biological productivity using the PISCES component of our coupled
847 model (Fig. 18). The results show a clear semi-annual cycle of Net Primary Production (NPP), New
848 Production (NP), and Regenerated Production (RP), which is consistent with the seasonal cycle of
849 nitrate and CHLa concentrations observed in the region (Körner et al., 2024). The highest values of
850 NPP (Fig. 17a) are found near the Congo River mouth (between 5.5°S and 6°S), where average values
851 exceed $0.20 \text{ mol N}\cdot\text{m}^{-2}\cdot\text{d}^{-1}$. During the main upwelling period (June–August), the NPP reaches its
852 maximum, with local peaks near 6°S exceeding $0.25 \text{ mol N}\cdot\text{m}^{-2}\cdot\text{d}^{-1}$. This intensity is comparable to,
853 though slightly lower than, the average primary production reported for the Benguela and Humboldt
854 systems, which reach 0.37 and $0.33 \text{ mol N}\cdot\text{m}^{-2}\cdot\text{d}^{-1}$ respectively (converted from Tilstone et al., 2009;
855 Monteiro et al., 2010).

856 The secondary upwelling period in December also shows high productivity, with NPP values reaching
857 approximately $0.22 \text{ mol N}\cdot\text{m}^{-2}\cdot\text{d}^{-1}$ near the river mouth. In contrast, during the downwelling periods
858 (notably in March and October), the system becomes less productive, with NPP dropping below
859 $0.075 \text{ mol N}\cdot\text{m}^{-2}\cdot\text{d}^{-1}$ in most of the coastal box. The analysis of production components reveals that
860 during the main upwelling season, the New Production (NP) (Fig. 17b) peaks at around
861 $0.15 \text{ mol N}\cdot\text{m}^{-2}\cdot\text{d}^{-1}$, representing about 50–60% of the NPP. In December, the NP contribution is
862 lower, around $0.10 \text{ mol N}\cdot\text{m}^{-2}\cdot\text{d}^{-1}$. The Regenerated Production (RP) (Fig. 17c) remains a significant
863 and stable driver of productivity throughout the year, particularly near the Congo mouth where it often
864 exceeds $0.125 \text{ mol N}\cdot\text{m}^{-2}\cdot\text{d}^{-1}$, highlighting the importance of nutrient recycling in this river-influenced
865 system.

866



867

868 **Figure 17:** Latitude-Time Hovmöller diagram of biological productivity: Net Primary Production (a), New
 869 Production (b) and regenerated Production (c) in the coastal box (6°S-3°S, 1° wide along the coastline). The
 870 units are milli mol per cubic meter per day.

871 High values of Net Primary Production (NPP) are also observed around 4.47°S, near the mouth of the
 872 Kouilou River, following the characteristic semi-annual cycle of the region. A detailed comparison of
 873 the production components (Fig. 17b, c) reveals that Regenerated Production (RP), fueled by the
 874 recycling of nutrients within the euphotic layer, is generally higher than New Production (NP). These
 875 two parameters remain consistent with the seasonal cycle of nitrate concentrations described
 876 previously.

877 The seasonal cycle of NPP in the Gabon-Congo system differs from those of the Namibia and
 878 Benguela upwellings, which are primarily wind-forced systems (Gutknecht et al., 2013). A key
 879 distinction lies in the efficiency of nitrate utilization: in our study area, the contribution of New
 880 Production to the total NPP is notably high. For instance, while the *f-ratio* (NP/NPP) in the Benguela
 881 system typically ranges between 0.2 and 0.4 (Monteiro et al., 2010), it reaches approximately 0.6 in
 882 the Gabon-Congo coastal box, indicating that more than half of the primary production is sustained by
 883 the upward supply of new nitrates.

884 Finally, we demonstrate that the conclusions regarding the nitrate budget are highly sensitive to the
 885 definition of the Mixed Layer Depth (MLD). In this study, we adopted a 3 m reference depth for the
 886 MLD calculation, following the criterion proposed by Aroucha et al. (2025). This shallower definition
 887 is more appropriate for the Gabon-Congo system, as it accurately captures the intense surface
 888 stratification induced by the river's freshwater plume. With this refined MLD criterion, our results
 889 show a significant shift in the balance of vertical processes: vertical diffusion (mixing) now emerges
 890 as the dominant mechanism supplying nitrate to the mixed layer, outweighing the contribution of

891 vertical advection. This finding aligns with recent observations in the Angolan upwelling (Brandt et
892 al., 2023; Körner et al., 2023, 2024) and the Gabon-Congo plume region (Scannell and McPhaden,
893 2018; Ngakala et al., 2025), which highlight turbulent mixing—often fueled by internal tides and
894 shear—as a major driver of vertical nutrient and heat fluxes. This shift emphasizes the critical role of
895 the 'Barrier Layer' and the strong surface halocline in trapping nutrients and modulating their upward
896 transfer through small-scale mixing processes rather than mean vertical motion.

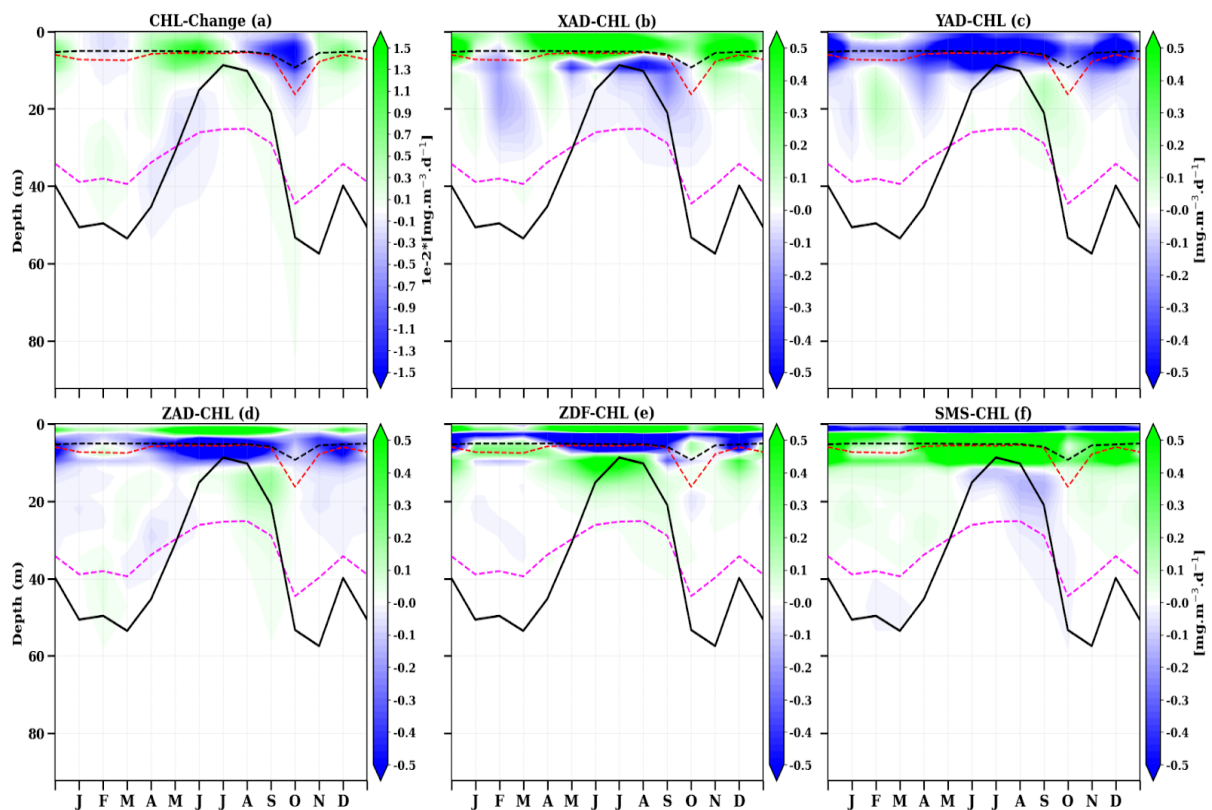
897 **5 Conclusion**

898 Throughout this work we have described and analysed the seasonal cycles in nitrate and CHLa
899 concentrations, as well as the physical and biological processes that modulate nitrate supply and
900 biological productivity in the mixed layer and in the euphotic layer in the Gabon-Congo upwelling
901 system. We began by validating a regional high-resolution ($1/36^\circ$) simulation of the coupled
902 physical-biogeochemical model NEMO-PISCES in this area for the studied year 2011. Surface and
903 subsurface validation of the simulation using observations (satellite, in situ, climatology) shows that
904 the model reasonably reproduces the main physical and biogeochemical characteristics of the study
905 area. Subsequently, the seasonal cycle of nitrate shows that there are two periods of upwelling and two
906 periods of downwelling (Fig. 4e,f and Fig. 11a). These upwelling and downwelling are associated with
907 remote forcing : Kelvin waves that propagate along the equator and the coastal waveguide force the
908 vertical migrations of the thermocline, which is also a proxy for the nitracline. The seasonal cycle of
909 CHLa is explained by that of nitrate. The assessment of the nitrate balance in the mixed layer shows
910 that the main nitrate is mainly supplied in the mixed layer by vertical diffusion (Fig. 10f), vertical
911 advection (Fig. 10d) and zonal advection (Fig. 10c), which is mainly modulated by nitrate inputs from
912 the Congo River at 6°S . The vertical advection induced by CTWs and vertical diffusion play also a
913 role in the nitrate supply, while nitrate losses are linked to meridional advection and the biological
914 activity (photosynthesis). In the lower part of the euphotic layer, on the other hand, nitrate is supplied
915 by zonal advection and vertical advection. Vertical diffusion contributes to nitrate losses, except in
916 downwelling periods where it represents one of the main drivers of nitrate supply. We have also seen
917 that meridional advection via the Angola Current, which transports the low-nitrate warm waters of the
918 Equatorial undercurrent, is the main driver of nitrate loss below the mixed layer throughout the year.
919 We find that vertical advection is controlled by the vertical nitrate gradient and nitrate input (Fig. 15),
920 rather than vertical velocity, when it brings nitrate into the mixed layer during the main upwelling
921 period. However, in the secondary upwelling in December, vertical advection also brings nitrate, but is
922 then mostly controlled by vertical velocity.

923 In future works, the interannual variability will be study especially associated with the interannual
924 variability of the Congo river discharges (Scannell and McPhaden (2018), Körner et al., 2023, 2024;
925 Brandt et al., 2023) and of the CTWs forced by the Equatorial Kelvin waves (e.g. Bachèlery et al.,
926 2015, 2016). Understanding the seasonal and interannual variability of productivity is of primary
927 interest to ensure the sustainability of ecosystems and fisheries in the Gabon-Congo upwelling system.

928 Appendix A : Euphotic Layer CHLa Budget Analysis

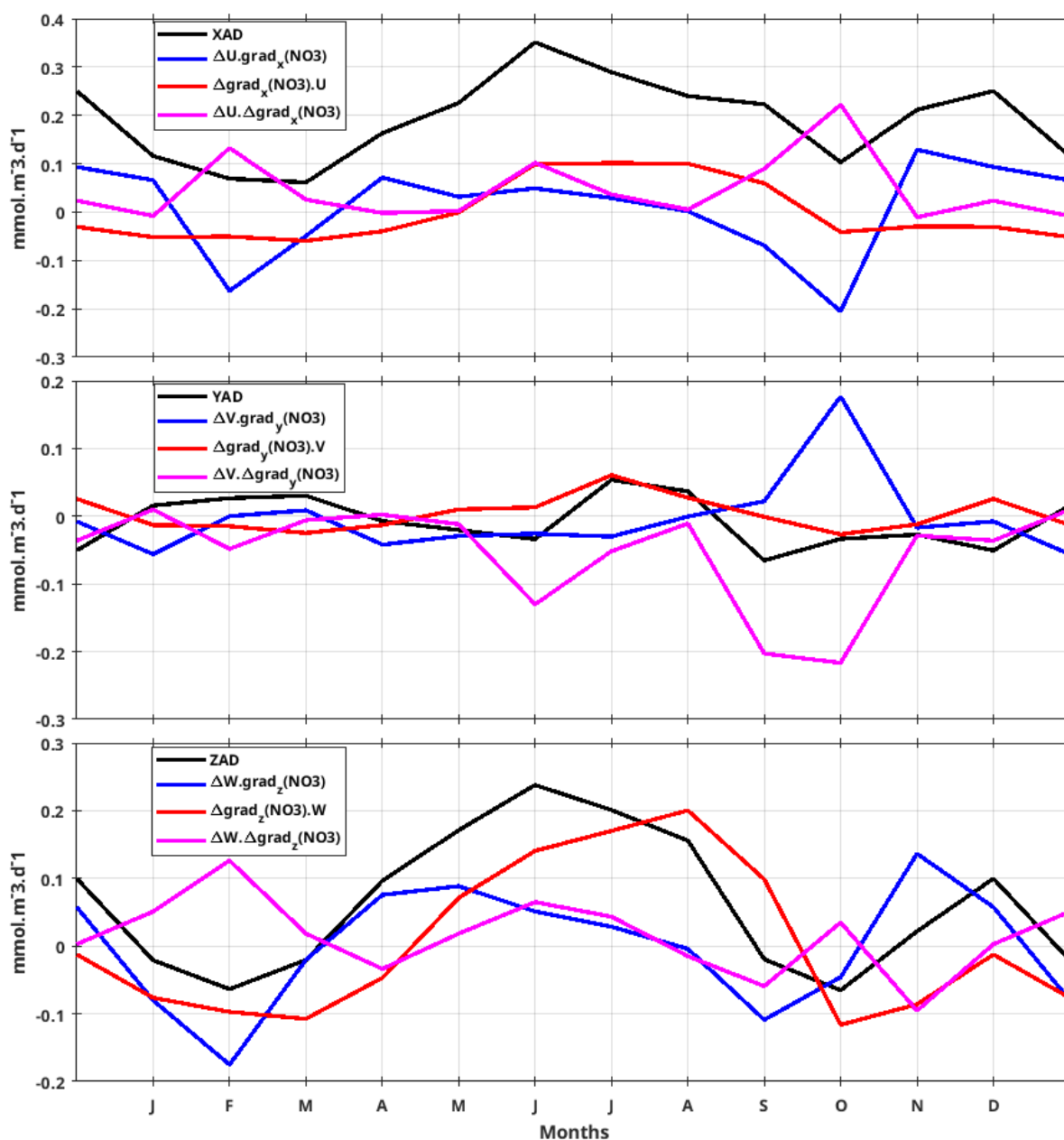
929 In the lower part of the euphotic zone, the CHLa budget (Fig. A1) is primarily governed by the
 930 interaction between coastal and offshore water masses. During the downwelling period, the zonal
 931 advection term (XAD_CHL) shows a net loss of CHLa near the base of the euphotic layer. This is
 932 explained by the passage of the South Equatorial Undercurrent (SEUC). As described by Nubi et al.
 933 (2016), undercurrent waters (EUC/SEUC) are relatively nitrate-poor and carry less CHLa than the
 934 highly productive coastal waters. The eastward transport of these offshore waters towards the
 935 Gabon-Congo coast leads to a dilution of the local CHLa concentration, a process captured by the
 936 negative values in the zonal advection budget.



937 **Figure A1:** Depth-time Hovmöller diagram of the seasonal chlorophyll-a budget along the Gabon-Congo coast
 938 (6°S–0°N, 1° coastal strip) for: (a) total rate of change (CHL-change), (b) zonal advection (XAD-CHL), (c)
 939 meridional advection (YAD-CHL), (d) vertical advection (ZAD-CHL), (e) vertical diffusion (ZDF-CHL), and (f)
 940 biological source-minus-sink term (SMS-CHL). Units for all panels are $\text{mg m}^{-3} \text{d}^{-1}$. The black solid line
 941 represents the thermocline (20°C isotherm), while dashed magenta, red and black lines indicate the euphotic,
 942 isothermal and mixed layer depths, respectively.

944 Appendix B : Euphotic Layer Nitrate Advections Components Analysis

945 To further investigate this relationship, the individual contributions of seasonal current and
 946 gradient variations are shown in **Appendix B (Fig. B1)**. This decomposition confirms that the
 947 mean flow acting on seasonal gradient anomalies is the dominant driver of advection variability.



948

949 **Figure B1:** Seasonal variation of advection components averaged in the euphotic layer, black line represent
 950 zonal, meridional and vertical advection in (a), (b) and (c) respectively. The red line in both three figures
 951 represents gradient variation, blue line is current variation and magenta line represents the simultaneous
 952 variation of gradient and current.

953 **Code and data availability.** Publicly available datasets were used for this study. Chlorophyll data
 954 (1998–2020) are from the Copernicus-GlobColour dataset (<https://doi.org/10.48670/moi-00281>,
 955 Copernicus, 2023a). The sea level anomaly data (1998–2020) were accessed via the Copernicus Server
 956 (<https://doi.org/10.48670/moi-00148>, Copernicus, 2023b). The MUR SST product created by the JPL
 957 MUR MEaSURES program as part of the GHRSSST (Group for High-Resolution Sea Surface
 958 Temperature) project is obtained from <https://podaac.jpl.nasa.gov/dataset/MUR-JPL-L4-GLOB-v4.1>
 959 (Chin et al., 2017) and ASCAT wind data <https://podaac.jpl.nasa.gov/dataset/ASCATB-L2-25km>. The

960 nutrient fields were assessed using the CSIRO Atlas of Regional Seas climatology (Dunn and
961 Ridgway, 2002) ,

962 <https://thredds.aodn.org.au/thredds/catalog/CSIRO/Climatology/CARS/2009/AODN-product/catalog.h>

963 [tml?dataset=CSIRO/Climatology/CARS/2009/AODN-product/](https://thredds.aodn.org.au/thredds/catalog/CSIRO/Climatology/CARS/2009/AODN-product/). Near surface currents from the

964 Ocean Surface Current Analysis Real-time (OSCAR, Johnson et al. 2007),

965 https://podaac.jpl.nasa.gov/dataset/OSCAR_L4_OC_INTERIM_V2.0. Model outputs are available

966 from the authors, especially GA, ID, GM, and JJ.

967

968 **Author contributions.** LJME outlined and wrote the paper. LJME and RDG produced the figures.

969 GM has run the NEMO-PISCES model. GA, ID, CYD the co-authors contributed to define

970 methodology and reviewed the paper.

971 **Conflict of Interest.** The authors declare that they have no conflict of interest.

972 **Acknowledgments.** Research is sponsored by the CNES SWOT-ETAO project (Surface Water and

973 Ocean Topography, Study of Ocean Topography and Altimetry by the National Centre for Space

974 Studies France). GENCI GEN7298 project (National High-Performance Computing Equipment) for

975 computing hours for simulations.

976 Thanks go to (<https://www.esr.org/research/oscar/oscar-surface-currents/>) to provide OSCAR current
977 data.

978 Also thanks to <https://podaac.jpl.nasa.gov/> for providing MUR SST data.

979 **Financial Support.** This project is funded by IRD-ARTS (Research Grant for a Thesis in the South

980 provided by Institute of Research for Development France) for my Phd scholarship.

981 **References**

982 Assene, F., Morel, Y., Delpech, A., Aguedjou, M., Jouanno, J., Cravatte, S., Marin, F., Ménesguen, C.,

983 Chaigneau, A., Dadou, I., Alory, G., Holmes, R., Bourlès, B., & Koch-larrouy, A. (2020). From

984 Mixing to the Large Scale Circulation : How the Inverse Cascade Is Involved in the Formation of the

985 Subsurface Currents in the Gulf of Guinea. 1-36. <https://doi.org/10.3390/fluids5030147>.

986 Aumont, O. and Bopp, L.: Globalizing results from ocean insitu iron fertilization experiments, Global

987 Biogeochem. Cy., 20, GB2017, <https://doi.org/10.1029/2005GB002591>, 2006.

988 Aumont, O., Belviso, S., and Monfray, P.: Dimethylsulfide (DMS) cycle with a 3-D

989 ocean-biogeochemical model, *Oceanogr. Lit. Rev.*, 11, 1637, <https://doi.org/10.1029/98GB02757>,

990 1998.

- 991 Aumont, O., Ethé, C., Tagliabue, A., Bopp, L., and Gehlen, M.: PISCES-v2: an ocean biogeochemical
992 model for carbon and ecosystem studies, *Geosci. Model Dev.*, 8, 2465–2513,
993 <https://doi.org/10.5194/gmd-8-2465-2015>, 2015.
- 994 Awo, F. M., Alory, G., Da-Allada, C. Y., Delcroix, T., Jouanno, J., Kestenare, E., and Baloitcha, E.: On
995 the seasonal and interannual variability of the sea surface salinity in the Gulf of Guinea, *Clim. Dynam.*,
996 60, 2121–2140, <https://doi.org/10.1007/s00382-022-06443-4>, 2023.
- 997 Awo, F. M., Rouault, M., Ostrowski, M., Tomety, F. S., Da-Allada, C. Y., and Jouanno, J.: Seasonal
998 cycle of sea surface salinity in the Angola Upwelling System, *J. Geophys. Res.-Oceans*, 127,
999 e2022JC018518, <https://doi.org/10.1029/2022JC018518>, 2022.
- 1000 Bachèlery, M. L. (2016). Variabilité côtière physique et biogéochimique en Atlantique Sud-Est: rôle du
1001 forçage atmosphérique local versus téléconnexion océanique (Doctoral dissertation, Ph. D. thesis,
1002 Toulouse: Laboratoire d'Etude en Géophysique et Océanographie Spatiale (LEGOS), University of
1003 Paul Sabatier, 215).
- 1004 Bachèlery, M.-L., Illig, S., and Dadou, I.: Interannual variability in the South-East Atlantic Ocean,
1005 focusing on the Benguela Upwelling System: Remote versus local forcing, *J. Geophys. Res. Oceans*,
1006 121, 284–310, <https://doi.org/10.1002/2015JC011168>, 2015.
- 1007 Bourlès, B., Molinari, R. L., Johns, W. E., Gouriou, Y., and Carder, K. L.: The South Equatorial
1008 Undercurrent in the Atlantic Ocean, *Geophys. Res. Lett.*, 31, L14301,
1009 <https://doi.org/10.1029/2004GL020020>, 2004.
- 1010 Brandt, P., Alory, G., Awo, F. M., Dengler, M., Djakouré, S., Imbol Koungue, R. A., Jouanno, J.,
1011 Körner, M., Roch, M., and Rouault, M. (2023). Physical processes and biological productivity in the
1012 upwelling regions of the tropical Atlantic. *Ocean Science*, 19(3):581–601,
1013 <https://doi.org/10.5194/os-19-581-2023>
- 1014 Cabos, W., Sein, D. V., Pinto, J. G., Koseki, S., Álvarez-García, F. J., & Durán-Quesada, A. M. (2017).
1015 The coastal upwelling system of the southeast Atlantic as simulated by a high-resolution coupled
1016 model. *Climate Dynamics*, 49(5), 1809–1828. <https://doi.org/10.1007/s00382-016-3319-9>
- 1017 Caniaux, G., Giordani, H., Redelsperger, J. L., Guichard, F., Key, E., and Wade, M.: Coupling between
1018 the Atlantic cold tongue and the West African monsoon in boreal spring and summer, *J. Geophys.*
1019 *Res.-Oceans*, 116, C04003, <https://doi.org/10.1029/2010jc006570>, 2011.
- 1020 Carr, M.-E. (2002). Estimation of potential productivity in Eastern Boundary Currents using remote
1021 sensing. *Deep Sea Research Part II: Topical Studies in Oceanography*, 49(1–3):59–80.
- 1022 Chavez, F. P., & Messié, M. (2009). A comparison of eastern boundary upwelling ecosystems.
1023 *Progress in Oceanography*, 83(1-4), 80-96.

- 1024 Chin, T.M, J Vazquez-Cuervo et E Armstrong (2017). "A multi-scale high-resolution analysis of global
1025 sea surface temperature". In : Remote sensing of environment 200, p. 154-169.
- 1026 de Boyer Montégut, C., Madec, G., Fischer, A. S., Lazar, A., and Iudicone, D.: Mixed layer depth over
1027 the global ocean: An examination of profile data and a profile-based climatology, *J. Geophys. Res.*
1028 *Oceans*, 109, C12003, <https://doi.org/10.1029/2004JC002378>, 2004.
- 1029 Dorothee Bonhoure, Elizabeth Rowe, Arthur J. Mariano, Edward H. Ryan. "The South Equatorial Sys
1030 Current." *Ocean Surface Currents*.(2004).
- 1031 <https://oceancurrents.rsmas.miami.edu/atlantic/south-equatorial.html>
- 1032 Dossa, A., Da-Allada, C., Herbert, G., & Bourlès, B. (2019). Seasonal cycle of the salinity barrier layer
1033 revealed in the northeastern Gulf of Guinea. *African Journal of Marine Science*, 41(2), 163–175.
1034 <https://doi.org/10.2989/1814232X.2019.1616612>
- 1035 Ducet, N., Le Traon, P.-Y., & Reverdun, G. (2000). Global high-resolution mapping of ocean
1036 circulation from TOPEX/Poseidon and ERS-1 and -2. *Journal of Geophysical Research*, 105(C819),
1037 19477–19498. <https://doi.org/10.1029/2000jc900063>
- 1038 Dunn, J. R. and Ridgway, K. R.: Mapping ocean properties in regions of complex topography, *Deep*
1039 *Sea Res. Part I*, 49, 591–604, [https://doi.org/10.1016/S0967-0637\(01\)00069-3](https://doi.org/10.1016/S0967-0637(01)00069-3), 2002.
- 1040 Estival, R., Quiniou, V., Messenger, C., 2013. Real-time network of weather and ocean stations:
1041 public-private partnership on in-situ measurements in the Gulf of Guinea. *Sea Technol.* 54 (3), 34–38.
- 1042 FAO: Fishery and Aquaculture Country Profiles, Angola, 2020, Country Profile Fact Sheets, Fisheries
1043 and Aquaculture Division [online], Rome, <https://www.fao.org/fishery/en/facp/ago?lang=en> (last
1044 access: 11 April 2023), updated 7 February 2022.
- 1045 Fréon, P., Barange, M., & Arístegui, J. (2009). Eastern boundary upwelling ecosystems: integrative
1046 and comparative approaches. *Progress in Oceanography*, 83(1-4), 1-14.
- 1047 Gutknecht, E., Dadou, I., Marchesiello, P., Cambon, G., Le Vu, B., Sudre, J., Garçon, V., Machu, E.,
1048 Rixen, T., Kock, A., Flohr, A., Paulmier, A., and Lavik, G. (2013). Nitrogen transfers off Walvis Bay:
1049 a 3-D coupled physical/biogeochemical modeling approach in the Namibian upwelling system.
1050 *Biogeosciences*, 10(6):4117–4135.
- 1051 Hardman-Mountford, N. J. and McGlade, J. S.: Retrieval of phytoplankton biomass from ocean colour
1052 in the Benguela ecosystem, *Remote Sens. Environ.*, 79, 11–23,
1053 [https://doi.org/10.1016/S0034-4257\(01\)00236-0](https://doi.org/10.1016/S0034-4257(01)00236-0), 2002.
- 1054 Hopkins, J., Lucas, M., Dufau, C., Sutton, M., Stum, J., Lauret, O., & Channelliere, C. (2013).
1055 Detection and variability of the Congo River plume from satellite derived sea surface temperature,

- 1056 salinity, ocean colour and sea level. *Remote Sensing of Environment*, 139, 365–385.
1057 <https://doi.org/10.1016/j.rse.2013.08.015>
- 1058 Hutchings, L., van der Lingen, C. D., Shannon, L. J., Crawford, R. J. M., Verheye, H. M. S.,
1059 Bartholomae, C. H., van der Plas, A. K., Louw, D., Kreiner, A., Ostrowski, M., Fidel, Q., Barlow, R.
1060 G., Lamont, T., Coetzee, J., Shillington, F., Veitch, J., Currie, J. C., and Monteiro, P. M. S.: The
1061 Benguela Current: An ecosystem of four components, *Prog. Oceanogr.*, 83, 15–32,
1062 <https://doi.org/10.1016/j.pocean.2009.07.046>, 2009.
- 1063 Johns, W. E., Brandt, P., Lumpkin, R., Fischer, J., Hormann, V., Pirani, A., Schmid, C., and Bourlès,
1064 B.: Variation of upper ocean seasonal and interannual velocity structure in the eastern equatorial
1065 Atlantic, *J. Phys. Oceanogr.*, 44, 1201–1212, <https://doi.org/10.1175/JPO-D-13-0132.1>, 2014.
- 1066 Johnson, E. S., Bonjean, F., Lagerloef, G. S., Gunn, J. T., & Mitchum, G. T. (2007). Validation and
1067 error analysis of OSCAR sea surface currents. *Journal of Atmospheric and Oceanic Technology*, 24(4),
1068 688-701.
- 1069 Jouanno, J.: Influence de la dynamique de l'Atlantique équatorial sur la variabilité de la langue froide,
1070 *PhD thesis*, Université de Toulouse III, <http://thesesups.ups-tlse.fr/1154/>, 2010.
- 1071 Kobayashi, S., Ota, Y., Harada, Y., Ebata, A., Moriya, M., Onoda, H., Onogi, K., Kamiguchi, H.,
1072 Kobayashi, C., Endo, H., Miyaoka, K., and Takahashi, K.: The JRA-55 Reanalysis: General
1073 specifications and basic characteristics, *J. Meteorol. Soc. Jpn.*, 93, 5–48,
1074 <https://doi.org/10.2151/jmsj.2015-001>, 2015.
- 1075 Kopte, R. (2017). The Angola Current in a Tropical Seasonal Upwelling System: Seasonal Variability
1076 in Response to Remote Equatorial and Local Forcing (Doctoral dissertation, Christian-Albrechts
1077 Universität Kiel).
- 1078 Körner, M., Brandt, P., and Dengler, M.: Seasonal cycle of sea surface temperature in the tropical
1079 Angolan Upwelling System, *Ocean Sci.*, 19, 121–139, <https://doi.org/10.5194/os-19-121-2023>, 2023.
- 1080 Körner, M., Brandt, P., and Dengler, M.: Seasonal cycle of sea surface temperature in the tropical
1081 Angolan upwelling system, *Ocean Sci.*, 19, 121–139, <https://doi.org/10.5194/os-19-121-2023>, 2023.
- 1082 Körner, M., Brandt, P., Illig, S., Dengler, M., Subramaniam, A., Bachèlery, M. Lou, and Krahnemann, G.:
1083 Coastal trapped waves and tidal mixing control primary production in the tropical Angolan upwelling
1084 system, *Sci. Adv.*, 10, 29–31, <https://doi.org/10.1126/sciadv.adj6686>, 2024.
- 1085 Locarnini, M. M., Mishonov, A. V., Baranova, O. K., Boyer, T. P., Zweng, M. M., Garcia, H. E., ... &
1086 Smolyar, I. (2018). World ocean atlas 2018, volume 1: Temperature.

- 1087 Koseki, S., Cabos, W., Sein, D. V., & Mohino, E. (2018). The role of the Gulf of Guinea upwelling in
1088 the atmospheric circulation of the tropical Atlantic in a high-resolution coupled model. *Climate*
1089 *Dynamics*, 51(3), 1017–1035. <https://doi.org/10.1007/s00382-017-3896-2>
- 1090 Koubanova, M., Koseki, S., & Keenlyside, N. S. (2018). Seasonal variability of the Atlantic cold
1091 tongue and its relationship with the Angola-Benguela upwelling system. *Climate Dynamics*, 51(7),
1092 2975–2993. <https://doi.org/10.1007/s00382-018-4197-0>
- 1093 Loukos, H. and Mémerly, L.: Simulation of the nitrate seasonal cycle in the equatorial Atlantic ocean
1094 during 1983 and 1984, *J. Geophys. Res.*, 104, 15549–15573, 1999.
- 1095 Madec, G. and the NEMO System Team, 2024. *NEMO Ocean Engine Reference Manual*, Zenodo.
1096 <https://doi.org/10.5281/zenodo.1464816>
- 1097 Messié, M., & Chavez, F. P. (2015). Seasonal regulation of primary production in eastern boundary
1098 upwelling systems. *Progress in Oceanography*, 134, 1-18.
- 1099 Monteiro, P., Dewitte, B., Scranton, M., Paulmier, A., and Van der Plas, A. (2011). The role of open
1100 ocean boundary forcing on seasonal to decadal-scale variability and long-term change of natural shelf
1101 hypoxia. *Environmental Research Letters*, (6):1–14.
- 1102 Ngakala, R. D., Alory, G., Da-Allada, C. Y., Dadou, I., Cardot, C., Morvan, G., ... & Baloitcha, E.
1103 (2025). Seasonal mixed layer temperature in the Congolese upwelling system. *Journal of Geophysical*
1104 *Research: Oceans*, 130(1), e2023JC020528.
- 1105 Nieto, K., & Mélin, F. (2017). Variability of chlorophyll-a concentration in the Gulf of Guinea and its
1106 relation to physical oceanographic variables. *Progress in oceanography*, 151, 97-115.
- 1107 Nubi, O., Bourles, B., & Edokpayi, C. (2016). On the Nutrient distribution and phytoplankton biomass
1108 in the Gulf of Guinea equatorial band as inferred from In-situ measurements. *Journal of*
1109 *Oceanography and Marine Science*, 7(1), 1-11.
- 1110 Ostrowski, M., da Silva, J. C. B., and Bazik-Sangolay, B.: The response of sound scatterers to El Niño-
1111 and La Niña-like oceanographic regimes in the southeastern Atlantic, *ICES J. Mar. Sci.*, 66,
1112 1063–1072, <https://doi.org/10.1093/icesjms/fsp102>, 2009.
- 1113 Radenac, M.-H., Jouanno, J., Tchamabi, C. C., Awo, M., Boursès, B., Arnault, S., and Aumont, O.:
1114 Physical drivers of the nitrate seasonal variability in the Atlantic cold tongue, *Biogeosciences*, 17,
1115 529–545, <https://doi.org/10.5194/bg-17-529-2020>, 2020.
- 1116 Resplandy, L., Hogikyan, A., Müller, J. D., Najjar, R. G., Bange, H. W., Bianchi, D., ... & Regnier, P.
1117 (2024). A synthesis of global coastal ocean greenhouse gas fluxes. *Global Biogeochemical Cycles*,
1118 38(1), e2023GB007803.

- 1119 Ridgway, K. R., J. R. Dunn, and J. L. Wilkin (2002), Ocean interpolation by four-dimensional least
1120 squares—Application to the waters around Australia, *J. Atmos. Oceanic Technol.*, 19, 1357–1375.
- 1121 Rouault, M.: Bi-annual intrusion of tropical water in the northern Benguela upwelling, *Geophys. Res.*
1122 *Let.*, 39, L12606, <https://doi.org/10.1029/2012gl052099>, 2012.
- 1123 Scannell, H. A. and McPhaden, M. J.: Seasonal mixed layer temperature balance in the southeastern
1124 tropical Atlantic, *J. Geophys. Res. Oceans*, 123, 5557–5570, <https://doi.org/10.1029/2018JC014099>,
1125 2018.
- 1126 Schott, F. A., Fischer, J., and Stramma, L.: Transports and pathways of the upper-layer circulation in
1127 the western tropical Atlantic, *J. Phys. Oceanogr.*, 28, 1904–1928, [https://doi.org/10.1175/1520-0485\(1998\)028<1904:TAPOTU>2.0.CO;2](https://doi.org/10.1175/1520-0485(1998)028<1904:TAPOTU>2.0.CO;2), 1998.
- 1129 Siegfried, L., Schmidt, M., Mohrholz, V., Pogrzeba, H., Nardini, P., Böttinger, M., and Scheuermann,
1130 G.: The tropical-subtropical coupling in the Southeast Atlantic from the perspective of the northern
1131 Benguela upwelling system, *Plos One*, 14, e0210083, <https://doi.org/10.1371/journal.pone.0210083>,
1132 2019.
- 1133 Sikhakolli, R., Sharma, R., Basu, S., Gohil, B. S., Sarkar, A., & Prasad, K. V. S. R. (2013). Evaluation
1134 of OSCAR ocean surface current product in the tropical Indian Ocean using in situ data. *Journal of*
1135 *earth system science*, 122(1), 187-199
- 1136 Sowman, M. and Cardoso, P.: Small-scale fisheries and food security strategies in countries in the
1137 Benguela Current Large Marine Ecosystem (BCLME) region: Angola, Namibia and South Africa,
1138 *Mar. Policy*, 34, 1163–1170, <https://doi.org/10.1016/j.marpol.2010.03.016>, 2010.
- 1139 Tchupalanga, P., Dengler, M., Brandt, P., Kopte, R., Macueria, M., Coelho, P., Ostrowski, M., and
1140 Keenlyside, N. S.: Eastern Boundary Circulation and Hydrography Off Angola: Building Angolan
1141 Oceanographic Capacities, *B. Am. Meteorol. Soc.*, 99, 1589–1605,
1142 <https://doi.org/10.1175/Bams-D-17-0197.1>, 2018a.
- 1143 Thiam, A., Alory, G., Jouanno, J., Da-Allada, C. Y., and Morvan, G.: Coastal upwelling in the
1144 Northern Gulf of Guinea: Seasonal cycle and mesoscale interactions, *Ocean Modelling*, 188, 102300,
1145 <https://doi.org/10.1016/j.ocemod.2024.102300>, 2024.
- 1146 Tilstone, G., Smyth, T., Poulton, A., and Hutson, R. (2009). Measured and remotely sensed estimates
1147 of primary production in the Atlantic Ocean from 1998 to 2005. *Deep Sea Research Part II: Topical*
1148 *Studies in Oceanography*, 56(15):918–930.
- 1149 Topé, G. D. A., Alory, G., Djakouré, S., Da-Allada, C. Y., Jouanno, J., & Morvan, G. (2023). How
1150 does the Niger River warm coastal waters in the Northern Gulf of Guinea? *Frontiers in Marine*
1151 *Science*, 10, 1187202. <https://doi.org/10.3389/fmars.2023.1187202>.

1152 Tuchen, F. P., Brandt, P., Lübbecke, J. F., and Hummels, R.: Transports and pathways of the tropical
1153 AMOC return flow from Argo data and shipboard velocity measurements, *J. Geophys. Res.-Oceans*,
1154 127, e2021JC018115, <https://doi.org/10.1029/2021JC018115>, 2022a.

1155 Voltaire, A., Belamari, S., & Lévy, M. (2019). On the role of ocean-atmosphere interaction in the
1156 onset of the Atlantic cold tongue. *Climate Dynamics*, 53(9), 5437–5455.
1157 <https://doi.org/10.1007/s00382-019-04717-0>

1158 Xu, Z., M. Li, C. M. Patricola, and P. Chang, 2014: Oceanic origin of southeast tropical Atlantic
1159 biases. *Climate Dyn.*, 43, 2915–2930, <https://doi.org/10.1007/s00382-013-1901-y>.

1160 Zeng, Z., Brandt, P., Lamb, K. G., Greatbatch, R. J., Dengler, M., Claus, M., and Chen, X.:
1161 Three-dimensional numerical simulations of internal tides in the Angolan upwelling region, *J.*
1162 *Geophys. Res.-Oceans*, 126, e2020JC016460, <https://doi.org/10.1029/2020JC016460>, 2021.

1163 Zuidema, P., Redemann, J., Haywood, J., Wood, R., Piketh, S., Hipondoka, M., & Formenti, P. (2016).
1164 Smoke and clouds above the southeast Atlantic: Upcoming field campaigns probe absorbing aerosol's
1165 impact on climate. *Bulletin of the American Meteorological Society*, 97(7), 1131-1135.

1166 Zweng, M. M., Seidov, D., Boyer, T. P., Locarnini, M., Garcia, H. E., Mishonov, A. V., ... & Smolyar,
1167 I. (2019). *World ocean atlas 2018, volume 2: Salinity*.

1168

1169